



**KTH Chemical Science
and Engineering**

Interactions of cellulose and model surfaces

Johanna Stiernstedt



Doctoral Thesis at the Royal Institute of Technology

Stockholm 2006

Akademisk avhandling som med tillstånd av Kungliga Tekniska Högskolan framlägges till offentlig granskning för avläggande av filosofie doktorsexamen den 24 februari 2006 klockan 10.00 i hörsal F3, Lindstedtsvägen 26, Stockholm

Johanna Stiernstedt, *Interactions of cellulose and model surfaces*

TRITA: YTK-0603

ISSN: 1650-0490

ISBN: 91-7178-260-5

Denna avhandling är skyddad enligt upphovsrättslagen. Alla rättigheter förbehålles.

Copyright © 2006 by Johanna Stiernstedt

All rights reserved. No part of this thesis may be reproduced by any means without permission from the author.

The following items are printed with permission:

PAPER I: © 2005 American Chemical Society

PAPER V: © 2005 American Institute of Physics

Tryckt hos Universitetsservice US AB, februari 2006.

Abstract

The focus of this thesis is fundamental surface force and friction studies of silica and cellulose surfaces, performed mainly with the atomic force microscope (AFM). The normal interactions between model cellulose surfaces have been found to consist of a longer range double layer force with a short range steric interaction, the nature of which is extensively discussed. Both the surface charge and range of the steric force depend on the type of cellulose substrate used, as does the magnitude of the adhesion. Studies of friction on the same surfaces reveal that surface roughness is the determining factor for the friction coefficient, with which it increases monotonically. The absolute value, however, is determined by the surface chemistry.

The above is illustrated by studies of the effect of adsorbed xyloglucan, a prospective paper additive, which is found in the cell wall of all plants. Xyloglucan is like cellulose a polysaccharide but the effect of its adsorption was to reduce the friction significantly, while following the identical trend with surface roughness. Xyloglucan also increases the adhesion between cellulose surfaces in a time dependent manner, interpreted in terms of a diffusive bridging interaction. These facts combined provide a mechanistic explanation to contemporaneous findings about xyloglucans benefit in paper strength and formation.

In air, the adhesion between e.g. particles or fibres, must be at least partially determined by the formation of capillary condensates. The dependence of capillary condensation on relative humidity is however not yet fully understood so studies have been performed to cast light on this phenomenon. Above about 60 % relative humidity the adhesion and friction increase dramatically due to the formation of large capillary condensates. The extent of the condensates depends both on the time the surfaces equilibrate, but also on the surface roughness. Harvesting of the condensate during shearing is also observed through hysteresis of the friction-load relationship.

Measurements of surface forces and friction in surfactant systems show a clear relation between the adsorbed surfactant layer and the barrier force and adhesion, which in turn determine the friction. All of these interactions are critically dependent on the composition of the surfactant solution. A mixed surfactant system has been studied consisting of a trimethylammonium cationic surfactant and a polyoxyethylene nonionic surfactant. The results are interpreted in terms of current theories of adsorption and synergistic interactions.

Finally, a novel technique for the *in situ* calibration and measurement of friction with the AFM is proposed. Comparison with lateral measurements show that the approach is successful.

Sammanfattning

Fokus för denna avhandling är fundamentala ytkrafts- och friktionsstudier av cellulosa och glasytor, utförda framför allt med atomkraftsmikroskop (Atomic Force Microscope, AFM). Normalkrafterna mellan modellytor av cellulosa har funnits bestå av långväga dubbelskiktskrafter och kortväga sterisk repulsion, vars natur diskuteras ingående. Både de lång- och kortväga krafterna är beroende av vilken typ av cellulosasubstrat som används samt storleken på adhesionen. Friktionsstudier på samma ytor visar att ytråheten bestämmer friktionskoefficienten, med vilken den ökar monotont. Det absoluta värdet på friktionskraften bestäms dock av ytkemin.

Ovanstående illustreras genom studier av effekten av adsorberad xyloglukan, ett nytt miljövänligt pappersstyrkemedel som finns naturligt i alla växter. Xyloglukan är, liksom cellulosa, en polysaccharid, men effekten av dess adsorption var att minska friktionen signifikant, samtidigt som trenden med ytråhet följdes. Xyloglukan ökar också adhesionen mellan cellulositytor, på ett tidsberoende sätt, vilket tolkas i termer av bryggbildande interaktion. Tillsammans ger dessa fakta en mekanistisk förklaring till de motsägelsefulla upptäckterna om xyloglukans fördelar för pappersstyrka och formation.

I luft måste adhesionen mellan t.ex. partiklar och fibrer, åtminstone till en viss del, bestämmas av kapillärkondensation. Kapillärkondensationens beroende av luftfuktigheten är dock inte helt klarlagt, så studier har genomförts för att närmare undersöka fenomenet. Över ca 60% relativ luftfuktighet ökar adhesionen och friktionen dramatiskt på grund av att stora kapillärkondensat bildas. Storleken på kondensaten beror på jämviktstiden, men också på ytråheten.

Mätningar av ytkrafter och friktion i tensidsystem visar ett tydligt samband mellan adsorberad mängd tensid och barriärkraft samt adhesion, vilket i sin tur bestämmer friktionen. Alla dessa krafter är avhängiga tensidlösningens sammansättning. Ett blandtensidsystem bestående av en katjonisk och en nonjonisk tensid har studerats och resultaten tolkas i termer av adsorption och synergieffekter.

Slutligen har en ny teknik för att mäta och kalibrera friktion med AFM föreslagits. Jämförelse med befintliga metoder visar att tillvägagångssättet är framgångsrikt.

Contents

List of Papers.....	2
1 Introduction.....	3
2 Surface forces	5
2.1 Van der Waals interaction.....	5
2.2 Electrostatic double layer force.....	5
2.3 DLVO theory and fitting of force curves	7
2.4 Non DLVO forces.....	8
2.5 Adhesion.....	8
2.6 Bridging adhesion.....	8
2.7 Capillary condensation.....	9
2.8 Friction.....	10
3 Surfactants in solution and at interfaces	11
3.1 Association of Surfactants	11
3.2 Adsorption at the solid-liquid interface.....	11
4 Experimental techniques	13
4.1 MASIF	13
4.2 AFM	15
4.3 Spring constant calibration	16
4.4 Deformable surfaces	17
4.5 Friction.....	18
5 Materials	21
5.1 Silica	21
5.2 Cellulose	21
5.3 Xyloglucan.....	21
5.4 Surfactants	22
6 Results and Discussion.....	23
6.1 Model surfaces	23
6.2 Surface modification.....	35
6.3 Technique development.....	45
7 Concluding remarks.....	50
8 Acknowledgements.....	52
9 References.....	53

List of Papers

- I. Forces between silica surfaces with adsorbed cationic surfactants: Influence of salt and added non-ionic surfactant**
Johanna Stiernstedt, Johan C. Fröberg, Fredrik Tiberg and Mark W. Rutland
Langmuir, **2005**, 21, 1875-1883
- II. Friction between cellulose surfaces and the effect of and xyloglucan adsorption**
Johanna Stiernstedt, Harry Brumer III, Qi Zhou, Tuula T. Teeri and Mark W. Rutland
Submitted to *Biomacromolecules*
- III. Cellulose model surfaces – a comparison**
Johanna Stiernstedt, Niklas Nordgren, Lars Wågberg, Derek G. Gray and Mark W. Rutland
Manuscript
- IV. Effect of capillary condensation on friction force measurements on cellulose, mica and silica substrates**
Adam A. Feiler, Johanna Stiernstedt, Katarina Theander, Paul Jenkins and Mark W. Rutland
Submitted to *Journal of the American Chemical Society*
- V. A novel technique for the in situ calibration and measurement of friction with the atomic force microscope**
Johanna Stiernstedt, Mark W. Rutland and Phil Attard
Review of Scientific Instruments, **2005**, 76, Art. No. 083710
Erratum
Review of Scientific Instruments, **2006**, 77, Art. No. 019901

Appendix:

Forces and Friction between silica surfaces in the presence of cationic and non-ionic surfactants

Johanna Stiernstedt and Mark W. Rutland
Manuscript in preparation

1 Introduction

Cellulosic fibres, being the load bearing polymer in plants and trees, figure in a wide range of applications, mainly within the textile and paper making industries, and there is a growing interest of using cellulose in composites. The behaviour of fibres in the final product and during manufacturing is crucially dependent upon the friction and adhesion interactions between individual fibres. However, from a fundamental point of view the underlying mechanisms are poorly understood even for model surfaces. The relation between friction and adhesion on a molecular level is as yet not well understood, and the dissipative mechanisms behind interfacial friction remain to a large extent unexplained. In addition, the roles of surface roughness and humidity are generally not quantitatively understood.

The AFM provides the opportunity to measure both normal surface forces and friction in direct connection to each other, which therefore can contribute to a deepened understanding of fundamental surface force and friction phenomena. Normal force measurements with the AFM are quickly performed, and with the development of the colloidal probe technique^{*1,2} a wide range of substrates have become available for force measurements; however the attachment of the colloidal probe adds a challenge to the measurement. Friction measurements with AFM are much more time consuming and the calibration of the torsional spring constant is nontrivial. Thus, it would be useful to have a technique for obtaining friction from normal force measurements, particularly if the calibration could be performed *in situ*, and technique development is thus an area with high priority and which is addressed in this thesis.

Cellulosic fibres have complicated morphologies, which has rendered fundamental studies such as direct surface force measurements difficult to say the least. An alternative to measurements on fibres is to develop and characterise suitable model surfaces. Glass has been used as a model surface for cellulose solely based on its hydrophilicity and acid/base character. Spin-coated cellulose surfaces have been used since 1993³ and also Langmuir-Blodgett deposited cellulose films.^{4,5} Cellulose spheres are very suitable as AFM colloidal probes and have been used since 1997.⁶⁻¹²

The strength of paper is governed by the interactions in the joint. Both lateral and normal forces are important. One of the factors affecting adhesion is capillary

* See section 4.2

condensation around the contact, but this phenomenon is poorly understood, and cellulose also changes its material properties in the presence of water. Complementary measurements on model surfaces with well defined surface chemistry and roughness thus gives an insight into the specific roles of these surface properties on the adhesion and friction in the presence of water condensates.

Paper (and joint) strength can be modified with additives, where starch and cationic polyelectrolytes are traditionally used, but a new generation of additives should be based on renewable resources. Also an additive needs to show benefit in more than one aspect if it is to be considered in an industry such as the paper one. The polysaccharide xyloglucan, which is present in the cell wall of all plants, has been experimentally added to pulp resulting in stronger and smoother paper.^{13,14} Its specific interaction with cellulose renders it an ideal candidate, and the possibility to perform enzymatic modification to add desired surface properties to the fibres makes it an exciting prospect.

The adhesion and friction between cellulose fibres is also of great importance in the manufacturing of viscose. In this application the friction in the spinning of fibres into yarn is modified by the use of a mixture of cationic and nonionic surfactants. (It is, however, crucial that the friction and adhesion not become too low, as the fibres will then separate and no yarn can be formed.) An investigation of the properties of adsorbed surfactant films, their dependence on composition and the relationship between barrier height and frictional properties would thus be useful in terms of understanding and optimizing this treatment.

2 Surface forces

Surface forces are forces experienced between two surfaces in close proximity or in contact. They generally operate over distances ranging from zero (contact) to about a hundred nanometres, although in some cases of so called hydrophobic interactions have been reported as having a range approaching micrometers. The nature of the forces depends strongly on the surface chemistry of the interacting bodies and of course on the nature of the medium in which they are immersed.

Quite a few different mechanisms for surface forces have now been identified and they can originate from surface charging, solvent packing effects, steric interactions and so on. Some of the relevant forces are briefly addressed below.

2.1 Van der Waals interaction

Van der Waals forces originate from fluctuations in the electron cloud of the atoms, which create temporary dipoles, and thus exist between all molecules. The van der Waals interaction, W , between two planes, at a distance, D , from each other, is described by the Hamaker constant, A , and it is given by

$$W = -\frac{A}{12\pi D^2} \text{ (per unit area).} \quad (2.1)$$

For two like surfaces the van der Waals interaction is always attractive. The Hamaker constant is characteristic for each set of surfaces interacting over a third medium.

2.2 Electrostatic double layer force

Outside a charged surface in water counterions will gather so that there is a higher counterion concentration near the surface than in the bulk solution which can be thought of as an ion cloud. This cloud, together with the surface layer of charge is known as the diffuse electrical double layer and the potential/ion distribution is described by the Poisson-Boltzmann (PB) equation:

$$\frac{d^2\psi(x)}{dx^2} = -\frac{e}{\epsilon\epsilon_0} \sum z_i n_{i\infty} \exp\left(-\frac{z_i e \psi(z)}{kT}\right) \quad (2.2)$$

where $\psi(x)$ is the electrostatic potential at distance x from the surface, z_i is the valency of the counterions, e is the elementary charge, $n_{i\infty}$ is the number density of ions in the

bulk solution, ε_0 the permittivity of vacuum, ε the dielectric constant of water, k is the Boltzmann constant and T is the temperature.

When two charged surfaces approach each other they experience a repulsive force due to overlap of the double layers. The force originates from entropy lost for the ions and can be described as an osmotic pressure, still it is called the electric double layer force. The electric double layer force is exponentially decaying with a decay length equal to the so called Debye length, κ^{-1} , which is a measure of the diffuse layer and depends solely on properties of the solution such as the salt concentration:

$$\kappa^{-1} = \left(\frac{\varepsilon \varepsilon_0 k T}{\sum_i e^2 z_i^2 n_{i\infty}} \right)^{1/2} \quad (2.4)$$

The potential distribution away from an isolated surface is (for symmetric $z:z$ electrolytes):

$$\psi(x) = -\frac{2kT}{ze} \ln \left[\frac{1 + \Gamma_0 \exp(-\kappa x)}{1 - \Gamma_0 \exp(-\kappa x)} \right] \quad (2.3)$$

where the surface potential, ψ_0 , is included through the relation $\Gamma_0 = \tanh(ze\psi_0/4kT)$.

The Grahame equation¹⁵ gives the relation between the surface potential and the surface charge, σ .

$$\sigma = \sqrt{8kT\varepsilon\varepsilon_0 n_{\infty}} \sinh\left(\frac{ze\psi_0}{2kT}\right). \quad (2.5)$$

Both the potential and the charge depend on the salt concentration in the bulk (and the valency of the salt). The surface charge generally increases with increasing salt concentration, while the surface potential generally decreases.

Experimentally it is impossible to measure the interaction between two flat surfaces. However, the Derjaguin approximation¹⁶ relates the interaction free energy per unit area, E_a , for two planes with the force, F_s , between two surfaces of higher curvature, for example spheres, through

$$E_a = \frac{F_s}{2\pi R} \quad (2.6)$$

where

$$R = \frac{R_1 R_2}{R_1 + R_2}, \quad (2.7)$$

and R_1 and R_2 are the radii for the two surfaces of higher curvature. The Derjaguin approximation is valid as long as the smallest radius is much bigger than the distance between the surfaces and the range of the interactions.

2.3 DLVO theory and fitting of force curves

The DLVO theory^{17,18} is a more or less classical theory aiming to describe the stability of colloidal sols and the interaction between macroscopic surfaces. It takes the van der Waals and the electric double layer forces into account, assuming that these are additive, which is an approximation that has been questioned¹⁹. Generally, the electrostatic repulsion dominates at large surface separations and the van der Waals attraction at small separations.

Fitting the DLVO theory to experimental data allows the apparent surface potentials of the interacting surfaces and the Debye length for the experiment to be achieved. The DLVO theory generally describes the forces between two surfaces very well down to small surface separations where other non-DLVO forces, such as hydration²⁰ and steric²¹ forces, become important. Yet, another approximation in the fitting procedure is made when the PB equation (Equation 2.2) is solved. Calculations of the interaction between two surfaces generally keep either the surface potential or the surface charge constant. In practice, keeping the potential or the charge constant correspond to two extremes; neither the potential nor the charge can be constant at the limit of small separations due to charge regulation. When two surfaces are pushed into molecular contact some ions are forced to condense on the surfaces, thus reducing the surface charge and the repulsion between the surfaces. In addition, the PB equation is valid for smeared out charges, and does not take discrete charges into account which becomes important at the limit of small surface separations. Thus there are several reasons why DLVO fits fail to describe the interactions at small surface separations.

2.4 Non DLVO forces

2.4.1 Hydration force

Oscillatory solvation forces arise between molecularly smooth surfaces due to the ordering and step-like removal of solvent molecules.¹⁵ For rough surfaces the oscillatory force is smoothed out and replaced by purely monotonic repulsive force. Hydration forces^{2,20} appear to arise between hydrophilic surfaces with strongly H-bonding surface groups or adsorbed hydrated ions. The energy required to remove the water molecules from the hydration shells results in a steep, strongly repulsive force.

2.4.2 Steric repulsion

Rough surfaces or surfaces with thermally mobile surface groups often exhibit repulsive forces due to entropic overlap of their various fluctuation modes. When polymeric molecules, attached to a surface, dangle out into the solution and are thermally mobile, then on approach of another surface the entropy of confining these dangling chains results in a repulsive entropic force.

2.5 Adhesion

Adhesion is a measurement of the energy required to separate two surfaces in a medium. The simplest treatment is that formulated with interfacial thermodynamics by Gibbs.²² In this treatment the energy required to separate two surfaces is determined solely by the surface energy of the surfaces and medium. For two dissimilar materials, the work of adhesion, W_{Adh} , is defined as,

$$W_{Adh} = \gamma_{ac} + \gamma_{bc} - \gamma_{ab} \quad (2.8)$$

where materials a and b interact in medium c , and γ_{xy} is the surface energy. For example hydrophilic surfaces are much more adhesive in air than in water. The adhesion may also be altered by polymers attached to the surface as further discussed in section 2.6.

2.6 Bridging adhesion

Polymer surfaces are often adhesive due to entropy gain as the number of possible low energy conformations available for polymer chains increases for the chains

crossing the midplane,²³ as the polymers gain entropy when two surfaces come into contact. Bridging adhesion, due to energetic binding,¹⁵ can occur between polymer surfaces when the polymer has large attraction to both surfaces. Bridging adhesion is relatively long range and has been measured as early as 1979.²⁴

2.7 Capillary condensation

In a humid atmosphere water will condense to droplets, preferably at the surface of hydrophilic materials. The critical radius of a droplet, the Kelvin radius (r_K), is determined by the relative humidity, RH, according to the Kelvin equation:

$$r_K = \frac{\gamma_L V}{RT \log(p/p_s)} \quad (2.9)$$

where γ_L is the surface tension of the liquid, V is the volume, R is the gas constant, T is the temperature and p/p_s is the vapour pressure divided by the saturated vapour pressure at 100% RH. Water does also condense in small annuli of hydrophilic material, as illustrated in **Figure 2.1**, creating a Laplace pressure, P , which is

$$P = \frac{\gamma_L}{r_K} = \gamma_L \left(\frac{1}{r_1} + \frac{1}{r_2} \right) \approx \frac{\gamma_L}{r_1} \quad (2.10)$$

where r_1 and r_2 are the two radii of the annulus. The pull-off force, F_{PO} , is:

$$F_{PO} = 4\pi R \gamma_L \quad (2.11)$$

where R is the radius of curvature for the force measuring system. Note that F_{PO} in Equation 2.11 is independent of the relative humidity and has shown to be valid for molecularly smooth mica surfaces over a considerable humidity interval. It has been shown for rough surfaces that this simple treatment is insufficient, and PAPER IV is largely devoted to studying the effects of roughness and exposure time on this phenomenon. A schematic picture of the formation of capillary condensates for rough surfaces is given in **Figure 2.1**.

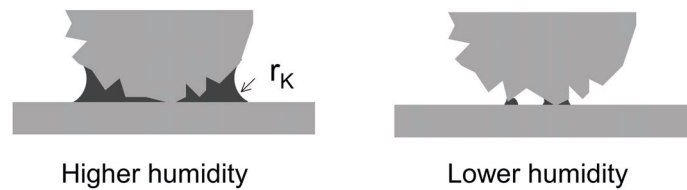


Figure 2.1. A schematic picture of the formation of capillary condensates for rough surfaces.

2.8 Friction

Friction occurs when two contacting surfaces are moved laterally with respect to one another, and is the result of energy dissipation associated with this movement as heat and sound are produced. Amontons' law is an empirical friction law, stating that the friction force is linearly dependent on the applied load, that fits surprisingly well to friction measurements performed on macroscopic surfaces under both lubricated and unlubricated conditions; it reads:

$$F_f = \mu L \quad (2.12)$$

where F_f is the friction force, μ is the friction coefficient and L is the applied load. According to Amontons' law the friction is independent of the contact area. In fact the reason that Amontons' law is valid is because macroscopic surfaces are rough. For rough surfaces the true contact area is dependent on the load, whereas the apparent contact area is constant. Measurements on molecularly smooth surfaces and single asperity contacts have shown that the friction force is dependent on the contact area and also on adhesion. Adhesion adds to the effective load such that:

$$F_f = \mu(L_{adh} + L) \quad (2.13)$$

where L_{adh} is the adhesion or pull-off force. Roughness decreases the adhesion so that it becomes less significant compared to the load and for rough surfaces with low adhesion Equation 2.13 reduces to Amontons' law.

Roughness decreases the adhesion and therefore the friction force, but it has been shown to increase the friction coefficient,²⁵⁻²⁷ an issue that is studied in PAPER III and IV.

3 Surfactants in solution and at interfaces

Surface active molecules, surfactants, are amphiphilic molecules, meaning that they have one part that is attracted to the solvent and another part repelling it. In aqueous solutions, the lyophilic part of a surfactant is referred to as the headgroup and the remaining as the hydrophobic tail. An effect of the amphiphility of the surfactants is that they tend to accumulate at interfaces, where the hydrophobic tails can escape from the aqueous surrounding.

3.1 Association of Surfactants

When the concentration of surfactants is sufficiently high, they associate into small aggregates, called micelles, in which the hydrophobic chains are shielded from contact with water by the hydrophilic head groups of the surfactants. This is as a result of the entropy gain (for the water molecules) associated with dispersing the “cage” of water which surrounds the hydrocarbon regions overcoming the entropy barrier (for the surfactants) to aggregation and repulsive forces such as charge repulsion between the headgroups. The concentration, at which micelle formation begins, is called the critical micelle concentration (*cmc*).

3.2 Adsorption at the solid-liquid interface

Surfactants often adsorb to solid surfaces. At hydrophobic surfaces, adsorption is noticeable already at low surfactant concentrations and the surfactants adsorb with the hydrophobic parts orientated towards the surface. However, on hydrophilic surfaces, adsorption occurs due to favourable interactions between the hydrophilic head groups and the surface, as well as favourable interaction between the surfactant's hydrophobic moieties. At low concentrations the surfactants adsorb flat to the hydrophilic surface, while at a higher concentration, the critical surface aggregation concentration, *csac*, aggregates form on the surface in much the same way as they do in bulk.

3.2.1 Proximal adsorption

Two interacting surfaces in liquid may actually induce adsorption of surfactants at very low surfactant concentrations, a phenomenon that has been recently measured called proximal adsorption.^{28,29} The adsorbed amount on one surface in the vicinity of

another surface is dependent on the distance between the surfaces and the change in adsorbed amount, $\Delta\Gamma_i$, follows:³⁰⁻³³

$$\Delta\Gamma_i = \Gamma_i(s) - \Gamma_i(\infty) = -\frac{1}{2} \left(\frac{\partial E_a}{\partial \mu_i} \right)_{T, p, \mu_j, s} \quad (3.1)$$

derived from the Gibbs adsorption equation. Γ_i is the adsorbed amount of component i on each surface, s is the distance between the surfaces, E_a is the interaction energy per unit area and μ_i is the chemical potential. This equation is valid when the temperature, T , pressure, p , chemical potential of the other components, μ_j , and the distance between the surfaces are constant. For an ionic surfactant, which adsorbs together with the counterion there is an additional factor $1/2$ on the right hand side.

4 Experimental techniques

4.1 MASIF

The development of the MASIF instrument (Measurement and Analysis of Surface Interaction Forces),^{34,35} a schematic of which is shown in **Figure 4.1**, was an attempt to measure surface forces between other surfaces than mica, which is essentially the only surface that can be studied in the surface force apparatus, SFA,³⁶ though other surfaces such as sapphire and silica have been used. As the surfaces in the MASIF do not have to be transparent, there is a larger variation in the range of substrates that may be investigated. The MASIF is also able to collect data at higher frequency than the SFA. What is lost compared to the SFA is, however, the absolute measure of the surface separation. Instead the surface separation is calculated from the constant compliance region or the region of hard wall contact, which is the region when both surfaces move at the same rate. An example of the raw data is given in **Figure 4.2** where the constant compliance and zero force regions are indicated. The position of zero separation is taken as the intercept between the constant compliance slope and the zero force line, as described by for example Senden.³⁷

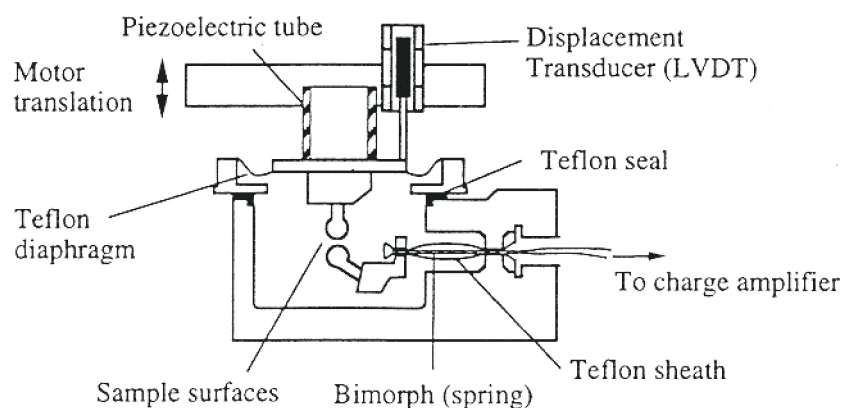


Figure 4.1 Schematic of the MASIF instrument.

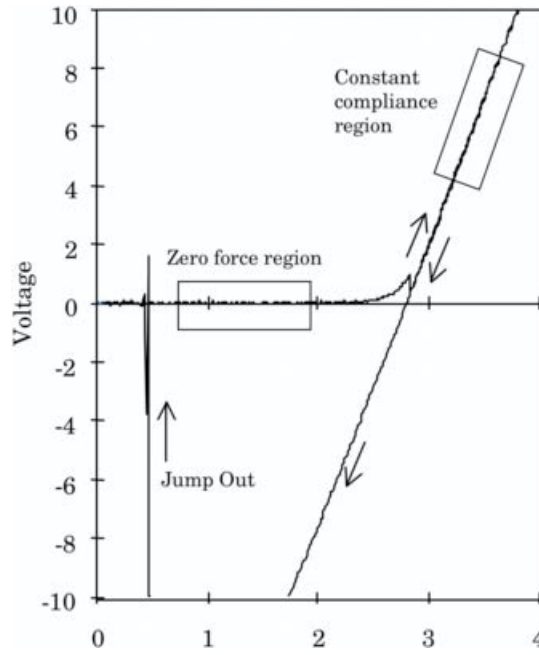


Figure 4.2 Raw data from the MASIF instrument.

To achieve control over the movement of both surfaces the upper surface is mounted on a piezoelectric tube, which is used to drive the surfaces and is mounted on a motorised stage, providing coarse positioning. The lower surface is mounted on a bimorph force sensor (which acts as an electronic spring), and its deflection is obtained from the charge of the surface of the bimorph. The two surfaces are mounted in a chamber, one below the other, as seen in **Figure 4.1**. The chamber is made from steel and Teflon, with silica windows, and its volume is approximately 10 ml. The chamber enables experiments to be run in both gaseous and liquid media. The bimorph force sensor is protected from the liquid in the chamber with a Teflon sheath. The motion of the piezoelectric tube is independently monitored using a linearly variable displacement transducer (LVDT) to compensate for the non-linearity in the expansion of the piezo with applied voltage. The only calibration needed is the sensitivity of the LVDT (which is determined interferometrically).

The substrates used are mainly glass spheres (of which the surfaces may be modified). The radii of the spheres and the spring constant of the bimorph force sensor are measured after each experiment, which allows the deflection to be converted to force over radius such that the Derjaguin approximation (Equation 2.6) can be applied. The slope of the constant compliance region converts the deflection in volts to nanometers, which is then multiplied with the spring constant and divided by the radius of interaction (as defined in Equation 2.7). The spring constant is

determined by placing small weights on the bimorph force sensor, and measuring the deflection by means of a travelling microscope.

4.2 AFM

The AFM³⁸ was designed to image surfaces and give height profiles. A cantilever, with a sharp tip, is brought into contact with a substrate mounted on a piezo electric tube, which expands and retracts in response to applied voltage. A laser beam is focused at the cantilever and reflected via a mirror to a photo sensitive detector, and the cantilever is deflected to a predetermined value of the detector. The substrate is then moved in the x-y direction and the cantilever follows the surface topography through z-movement of the piezo electric tube. A feed-back loop ensures that the cantilever is kept at constant deflection and the z-movement of the piezo electric tube is recorded.

The AFM can also be used to measure surface forces in which case the piezo electric tube is moved a predetermined distance only in the z-direction and the force is obtained from the deflection of the cantilever as described for the MASIF data, a thorough description is also given in ref³⁷. The cantilever tip is very sharp which is good for imaging, but it is difficult to accurately obtain the curvature which is required for interpreting the force data, for example through the application of the Derjaguin approximation (Equation 2.6). (The radius of curvature is also on the borderline of being too small for the Derjaguin approximation to be valid.) Now with the colloidal probe technique,^{1,2} which uses a spherical colloidal probe instead of a tip on the cantilever, the radius of curvature is well defined, as measured by means of a light microscope (Nikkon), and force measurements are quantitative. A schematic of the AFM is show in **Figure 4.3**.

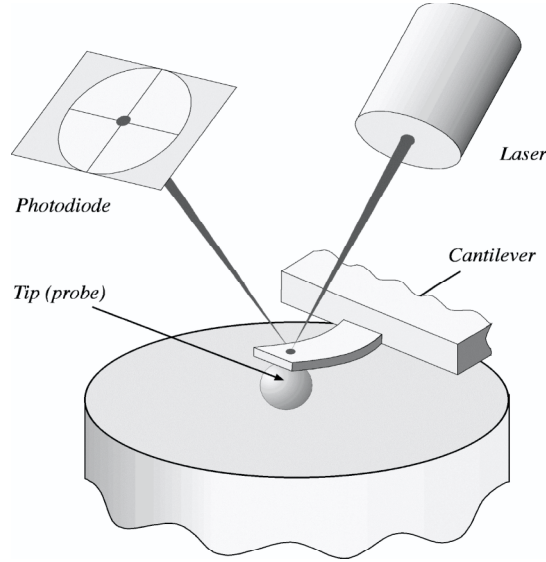


Figure 4.3. The AFM set-up in colloidal mode configuration. Picture by courtesy of Lachlan Grant.

4.3 Spring constant calibration

In order to quantify the measured interaction the AFM cantilever must be calibrated in that the spring constant is determined. There are currently two widely used methods to determine the spring constant, namely the added mass method³⁹, and the thermal method⁴⁰⁻⁴³. In the added mass method, small weights (typically tungsten spheres) are placed on the cantilever at the position of the colloidal probe, and the resonant frequency measured. The resonant frequency, ω_f , is related to the added mass, m_i , by

$$\omega_f^2 = \frac{k_z}{4\pi^2(m_0 + m_i)} \quad (4.1)$$

where k_z is the normal spring constant, and m_0 is the effective mass of the cantilever.

Also in the thermal method, the unloaded resonant frequency for the cantilever is measured, together with the quality factor, Q_f and the spring constant is calculated by

$$k_z = 0.1906\rho b^2 L Q_f \omega_f^2 \Gamma_i^f(\omega_f) \quad (4.2)$$

where ρ is the density of the surrounding media (usually air), b and L are width and length of the cantilever, respectively, and Γ_i^f is the imaginary component of the hydrodynamic function given by Equation 20 of Ref⁴⁴. This method requires high

frequency data acquisition, and has become more used as computers have become faster.

4.4 Deformable surfaces

Generally materials deform elastically when exposed for an applied load. This deformation may be calculated using the Hertz theory⁴⁵, which predicts the contact area, a , and central displacement, δ , for two non-adhering surfaces in contact.

$$a^3 = RF / K \quad (4.2)$$

$$\delta = a^2 / R = F / Ka \quad (4.3)$$

$$\frac{1}{K} = \frac{3}{4} \left[\frac{1 - \nu_1^2}{E_1} + \frac{1 - \nu_2^2}{E_2} \right] \quad (4.4)$$

where R is the radius of curvature, F is the applied force, K is the reduced elastic modulus, δ_n is the poisson ratio for each surface and E_n is the elastic modulus for each surface. For adhesive surfaces, the Hertz theory has been modified in the JKR⁴⁶ and DMT⁴⁷ theories.

The best way to analyse the force between deformable particles is to use the method of Rutland *et al.*⁴⁸ and measure the deflection sensitivity of a bare cantilever against a hard surface *in situ* and then move the cantilever to the deformable substrate of interest, e.g. a cellulose sphere. Now, this method does not allow for symmetrical cellulose-cellulose interactions to be measured for example, since one of the deformable surfaces is attached to the cantilever. An alternative route is to measure the deflection sensitivity in a calibration measurement before gluing the probe to the cantilever, however, the deflection sensitivity is sensitive to the position of the cantilever relative to the laser, and to the exact pathway of the laser light. Yet another way to treat this experimentally is to use the elastic modulus of the material and fit Hertz theory to the force, as shown in **Figure 4.4**. Deformation of the substrates will, if not taken into account in the analysis, be manifested as a repulsion (as dashed line in **Figure 4.4**) which increases with increasing softness of the materials.

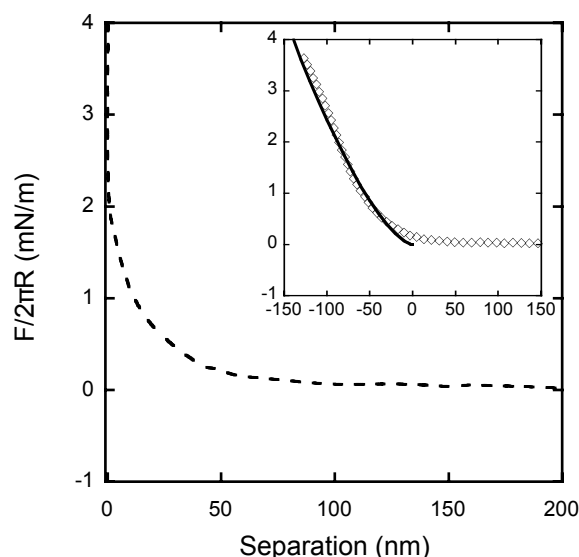


Figure 4.4. AFM analyse of a deformable surface. Forces on approach between a cellulose sphere and a very soft solvent cast cellulose film in a solution of 0.1 mM NaCl. The dashed line shows conventional analysis and the diamonds in the inset show the recalculated force with a fit of Hertz theory with $K = 1.7$ MPa (solid line). For clarity only every 20th data point is plotted.

Another problem in systems with deformable materials is to determine the position of zero separation, as intimate contact is not marked by a sharp discontinuity in the slope of the force curve. Instead there is a gradual increase in the repulsion between the surfaces prior to their coming into intimate contact. Rutland *et al.*⁴⁸ use the first point after the van der Waals jump as zero of separation, however this is not practicable for measurements in water where no van der Waals attraction is seen on approach. If the surface potential is known, DLVO fitting may be used to determine zero separation.

4.5 Friction

In traditional friction measurements the cantilever scans the surface laterally at increasing loads while the response in the lateral detector is recorded. The friction between the surfaces causes the cantilever to deflect laterally and a typical friction loop is shown in **Figure 4.5**. The friction voltage is half the difference between the two traces of the friction loop and it is plotted versus the actual applied load to achieve a typical friction – load trace, the slope of which is the friction coefficient.

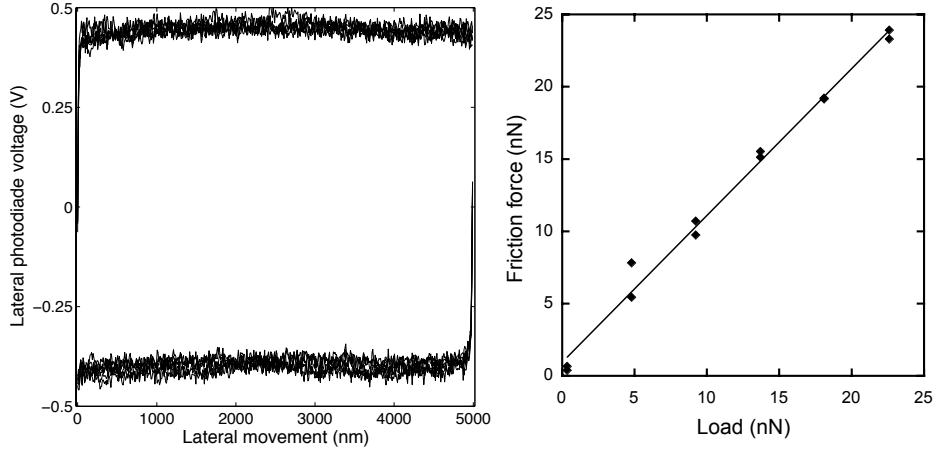


Figure 4.5. Left panel: Example of a friction loop (6 lines). Right panel: Friction force plotted versus applied load. The slope of the line equals the friction coefficient.

The quantification of the friction results is, however, nontrivial. The torsional calibration is a time consuming issue; often as much time is spent on the calibration as on the measurement itself. The methods that have been proposed over the years depends either on an *ex situ* calibration⁴⁹⁻⁵², or on calculations of material properties⁵³⁻⁵⁷. In the *ex situ* calibration a torque is applied at one side of free end of the cantilever, as illustrated in **Figure 4.6**, meanwhile the lateral voltage, ΔV_{lat} , as well as the normal (vertical) voltage, ΔV_{vert} , are recorded. The friction calibration factor, γ_f , is then calculated by

$$\gamma_f = \alpha k_z L \frac{\Delta V_{vert}}{\Delta V_{lat}} \quad (4.3)$$

where α is the deflection sensitivity, k_z is the normal spring constant, and L is the distance from the centre of the cantilever to the point of applied torque. To achieve the torsional spring constant, k_θ , requires measurement of the lateral sensitivity of the detector, β ,⁴⁹ then

$$k_\theta = \gamma_f \beta \quad (4.4)$$

The torsional spring constant is calculated from material properties by

$$k_\theta = \frac{Gbt^3}{3L} \quad (4.5)$$

where G is the shear modulus, b , L and t are width, length and thickness of the cantilever, respectively. However, since the cantilevers are very thin the thickness is

usually difficult to determine accurately. A new method to measure and calibrate friction *in situ* is proposed in section 6.3 and more thoroughly in PAPER V.

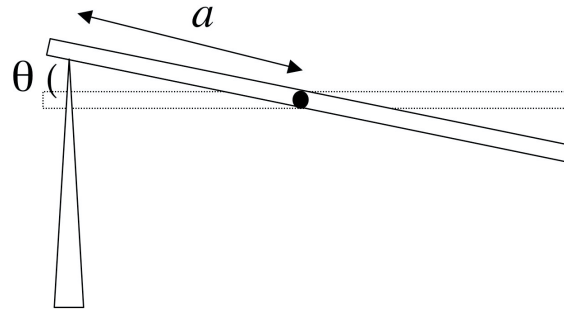


Figure 4.6. A rectangular AFM cantilever seen from its free end. A torque is applied at a distance a from the centre of the cantilever, causing the cantilever to twist an angle θ .

5 Materials

5.1 Silica

Glass surfaces of spherical curvature used in the MASIF measurements were made, immediately before use, by melting one end of a 2-cm long glass rod of 1 mm radius, which gives a hemisphere with a radius of about 2 mm. The rms roughness, as measured by AFM imaging, is in general below 0.1 nm for a scan size of 1 x 1 μm .⁵⁸

Polished silicon wafers with a thermally oxidised layer being 170 nm were kindly provided by Dr. Stefan Klintström, University of Linköping, Sweden. Cleaning was performed in a mixture of 25% NH_4OH , 30% H_2O_2 and H_2O (1:1:5, by volume) at 80°C for 10 min, followed by cleaning in a mixture of 25% HCl , 30% H_2O_2 and H_2O (1:1:5, by volume) at 80°C for 10 min. The wafers were subsequently rinsed in Milli-Q water and then in ethanol.

Silica beads (Duke Scientific Corporation, USA) were attached in-house on uncoated, tipless, rectangular silicon cantilevers (MicroMasch, Tallinn, Estonia) with Casco Araldite Rapid epoxy adhesive. Prior to use the cantilevers were rinsed in Milli-Q water and ethanol.

5.2 Cellulose

Regenerated cellulose spheres (Kanebo, Japan) made by the viscose process were used both as colloidal probes and as the lower surface glued to mica surfaces. Also other cellulose surfaces were used, namely spin-coated cellulose surfaces made from NMMO⁵⁹ (either neat or annealed overnight at 105°C), and nanocrystalline cellulose surfaces.^{60,61} The surface roughness of the cellulose surfaces was investigated in PAPER III and is presented in **table 6.1** in section 6.1.1.

5.3 Xyloglucan

Xyloglucan (XG) from tamarind (*Tamarindus indica*) seed (Megazyme, Bray, Ireland) had a monosaccharide composition of Xyl:Glc:Gal:Ara = 35:45:16:4, according to the supplier's specification. Xyloglucan was dissolved in Milli-Q water (1 mg/mL) and was allowed to adsorb to cellulose materials overnight. The structure of xyloglucan is shown in **Figure 5.1**.

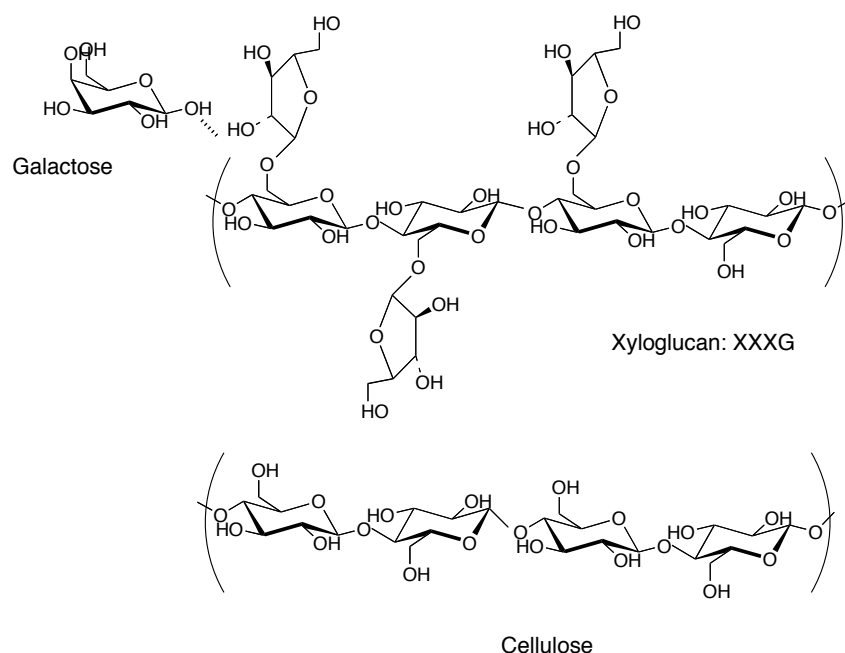


Figure 5.1. Structure of xyloglucan and cellulose.

5.4 Surfactants

Two surfactants, a cationic and a nonionic, and mixtures of these have been studied in this thesis. Both of the surfactants, which are displayed in Figure 4.1, have 14 carbons in their hydrocarbon tails, but their cmc's differ with two orders of magnitude due to their different headgroups. The cationic surfactant, tetradecyltrimethylammonium bromide (TTAB), has a cmc of $3.5 \times 10^{-3} \text{ M}$ ^{62,63}, whereas the nonionic surfactant, hexa-ethylene glycol mono n-tetradecyl ether (C_{14}E_6), has a cmc of $1 \times 10^{-5} \text{ M}$ ⁶².

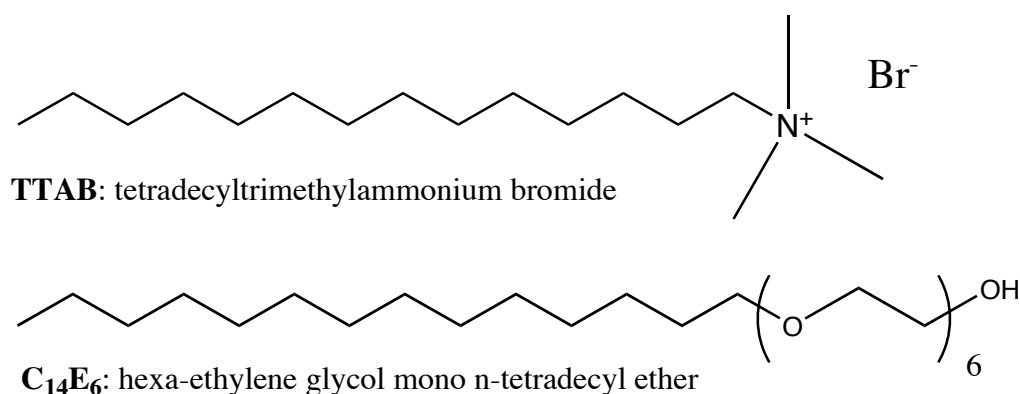


Figure 5.1 Structures of the surfactants studied in this thesis.

6 Results and Discussion

6.1 Model surfaces

Model surface are crucial for fundamental research about surface interactions. Mica is classically the most studied surface due to its molecular smoothness and suitability for the SFA, which require transparent surfaces. However silica and glass surfaces have become equally studied in connection to the development of the AFM colloidal probe technique, since they are available in a variety of morphologies, such as spheres and plates. With the colloidal probe technique also the forces between many other materials can be studied given that the radius of interaction is well defined. In the case of cellulose spherical and flat surfaces may be investigated relatively easily, but cellulose fibres are more difficult.

6.1.1 Cellulose

A number of cellulose surfaces have been studied (in PAPER II and III) by means of AFM colloidal probe technique, with a cellulose sphere as colloidal probe. The lower surface, attached to the driving piezocrystal was either a cellulose sphere glued to a mica surface, a spin-coated cellulose surface made from NMMO⁵⁹ (either neat or annealed overnight at 105°C), a nanocrystalline cellulose surface,^{60,61} or a silica surface.

Figure 6.1 shows the normalized force-distance profiles between a cellulose spheres and the different cellulose surfaces in solutions of 0.1 mM NaCl. The figure is explained in some detail since the features here are preset in most of the subsequent force curves shown in the thesis. The curves are qualitatively very similar for the four surfaces. At longer range a double-layer interaction is present indicating that the surfaces are charged. In all cases the lines are fits of DLVO theory^{17,18} to the data (the solid line represents a fit using the boundary condition of constant surface charge and the dashed line the boundary of constant potential). All fits had a Debye length of 30 nm, which is the calculated value for 0.1 mM salt, and hence not a fitting parameter, and a Hamaker constant⁶⁴ of 8×10^{21} J. The sign of the potential cannot be directly obtained from the DLVO fitting, but zeta-potential measurements of cellulose show that cellulose is negatively charged above pH 3.⁶⁵ At small surface separations a short-range repulsion was observed in all cases, which has also been observed previously for cellulose,^{3,7,8,12} and is further discussed in PAPER II and III.

Two theories of the origin of this short-range repulsion are currently discussed in the literature. One model argues that the repulsion is caused by compression of a highly solvated (swollen) surface layer of the cellulose, and the other model interprets the repulsion as a result of overlapping charged polymeric chains extending from the cellulose surfaces, in other words an electrosteric repulsion. In fact, any argument which supports an electrosteric force is equally appropriate to a swollen layer and vice versa, so it is really not possible to distinguish between these two models. For the sake of simplicity, this force component is here referred to as a steric or electrosteric force.

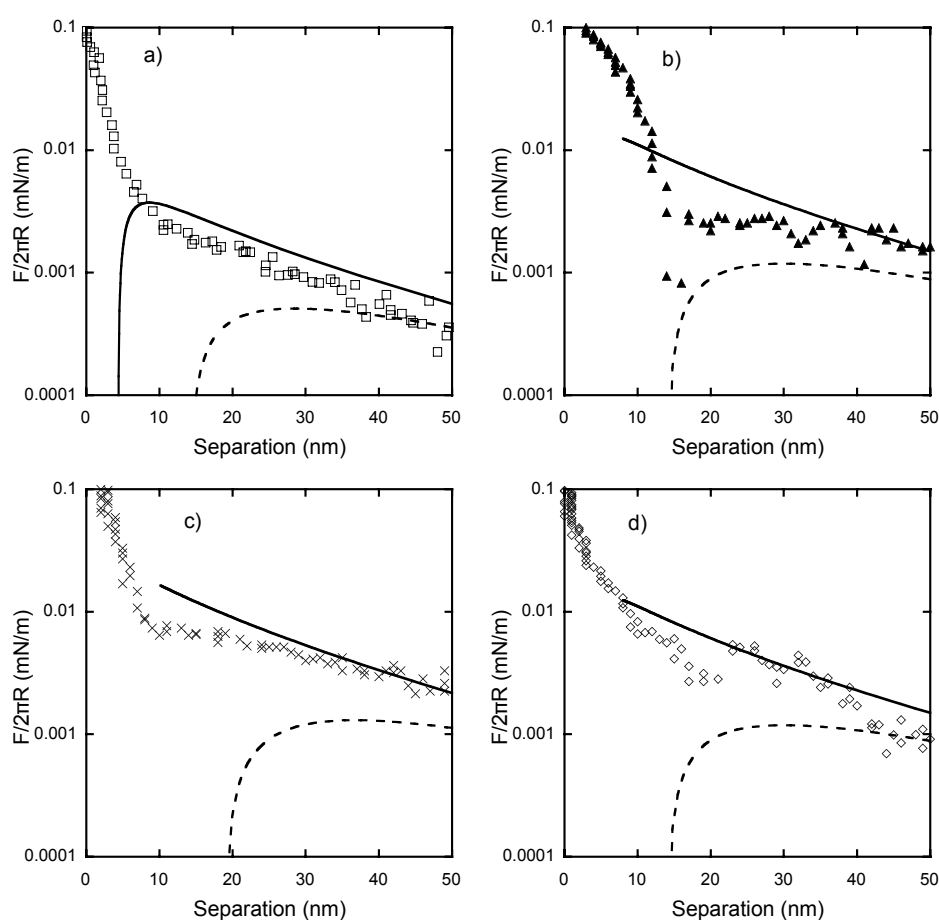


Figure 6.1. Normalized force profiles between a cellulose sphere and **a)** another cellulose sphere, **b)** a neat spin-coated cellulose surface, **c)** an annealed spin-coated cellulose surface, and **d)** a nanocrystalline cellulose surface, all immersed in 0.1 mM NaCl solutions. The lines are fits of DLVO theory to the data with Debye length 30 nm (calculated value, not a fitting parameter) and Hamaker constant 8×10^{21} J. The solid line represents the constant charge boundary condition, and the dashed line the boundary of constant potential. The fitted surface potentials are: a) -8 mV, b) -8/-18 mV, c) -8/-25 mV, d) -8/-18 mV.

The force profile between the two spheres (**Figure 6.1 a**) is approaching the resolution of the instrument and the curve shown is thus the average of ten consecutive force runs. In this case the results were fitted using the symmetrical form⁶⁶ of DLVO theory. The fitted surface potential for the two surfaces is -8 mV and thus -8 mV has been used as the potential for the cellulose sphere in all the other fits. The plane of charge has been assumed to lie at zero separation, but presumably the charge is in fact spread out over the compressible layer, so this is at best an approximation. The range of the steric force is interpreted as being the point at which the curve deviates repulsively from the double-layer behaviour and this can be seen to be about 10nm.

Figure 6.1 b shows the force profile between a cellulose sphere and a neat spin-coated cellulose surface. The forces between these two different cellulose materials were fitted using the asymmetric^{67,68} form of DLVO theory (which was also used for the other asymmetrical surface combinations) and the fitted potential for the neat spin-coated cellulose surface is -18 mV. In this case a very small attractive force was observed prior to the onset of the steric repulsion at a surface separation of about 15 nm. The attractive force is a van der Waals interaction which seems reasonably consistent with the predictions of DLVO theory. In general this attraction seems to be screened by the steric force.

The force profile between a cellulose sphere and an annealed spin-coated cellulose surface is shown in **Figure 6.1 c**. The fitted surface potential is -25 mV for the annealed spin-coated surface and the onset of the steric is slightly less than 10 nm, which shows that the surface potential increases with annealing, whereas the steric repulsion decreases. Presumably the effect of annealing is to drive out water and force the cellulose to form hydrogen bonds – related to the so called “hornification” process – and the result of this is that the solubility of the surface chains is commensurately less, or at least the time taken for the surface to swell is much longer. It is less clear why the apparent potential should increase, this may be related to the formation of a better defined plane of charge.

The forces between a cellulose sphere and a solvent-cast nanocrystalline cellulose film are shown in **Figure 6.1 d**. The fitted surface potential is intermediate between that of the sphere and that of the solvent cast films at -18 mV. The major difference is that a more pronounced van der Waals attraction is observed for the nanocrystalline cellulose. The onset of the steric repulsion is not as well defined as in the other cases but is best estimated as 20 nm, where the van der Waals minimum is. A more

crystalline surface would be expected to have less swelling and less compressibility and it is therefore not unexpected that the van der Waals forces are more clearly manifested in this case. It is therefore surprising that the steric force is actually the longest ranged of all! After the nanocrystalline surface had been in water over night, the forces became very long-range and the deflection sensitivity had increased significantly, which is a sign that the surface have become soft, probably because of major swelling or delamination indicating that there is some doubt about the long-term stability of these surfaces.

Figure 6.2 shows the forces measured on separation of two cellulose spheres in a solution of 0.1 mM NaCl. A small adhesion is observed on separation; the surfaces jump apart from a position 5 nm out from hard wall contact. The arrow, indicating the jump out of contact, has a slope 50 kN/m², which corresponds well to the cantilever spring constant (0.2 N/m) divided by the radius of interaction (3.69 μ m). The jump out is due to a spring instability which occurs when the energy stored in the spring is greater than the adhesive force. Thus the points recorded by the instrument, with 2.5 ms interval, have a gradient corresponding to the spring constant. The surfaces jump apart into an attractive force profile, which follows van der Waals predictions (solid line) with a Hamaker constant of 8×10^{-21} J⁶⁴ and the plane of interaction placed at the point of maximum adhesive force (which is 3 nm from nominal hard wall contact). On approach of the surfaces there is compression and dehydration of the water swollen surface layer. During the time scale of the separation the cellulose is not able to re-hydrate, which is why the measurement is slightly hysteretic.

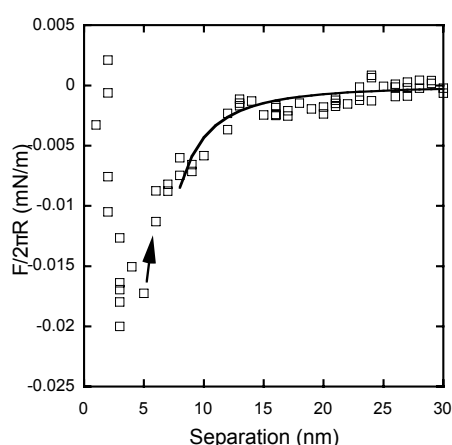


Figure 6.2. Force curve on separation between two cellulose spheres in a solution of 0.1 mM NaCl. The solid line is a fit of van der Waals theory with a Hamaker constant of 8×10^{-21} J. The arrow, which has a slope identical to the spring constant, indicates the jump out of contact.

The adhesion for the spin-coated surfaces is in good agreement with **Figure 6.2**, whereas the nanocrystalline surface shows larger adhesion, which is in good agreement with both the larger attraction seen on approach, and the lower surface roughness for the nanocrystalline surface.

Friction force versus load data for the different surfaces is presented in **Figure 6.3**. The friction behaviour for all surfaces follows Amontons' law (Equation 2.12). Before any comparison is made it is worth noting that all the substrates are sufficiently robust to withstand the shearing and loading, at least under the rather benign conditions applied here. Were there to be any damage of the films during the friction measurements this would be observed as a well defined breakpoint in the friction-load relationship as the nature of the contact changed.

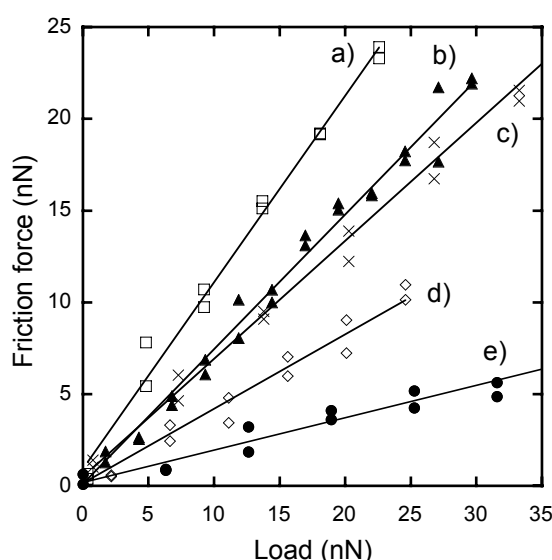


Figure 6.3. Friction measurements between a cellulose sphere and a) another cellulose sphere (open squares), b) a neat spin-coated cellulose surface (closed triangles), c) an annealed spin-coated cellulose surface (crosses), d) a nanocrystalline cellulose surface (open diamonds) and e) a silica plate (closed circles), all immersed in 0.1 mM NaCl solutions. The solid lines represent the friction coefficients, which are a) $\mu = 1.02$, b) $\mu = 0.74$, c) $\mu = 0.64$, d) $\mu = 0.41$, and e) $\mu = 0.18$.

Despite the fact that in every case, except e), the contact is ostensibly cellulose-cellulose the friction coefficients vary quite significantly, underlining the point that there is no intrinsic friction coefficient that is characteristic of a material *per se*. The friction coefficient is very sensitive to the surface roughness.²⁵⁻²⁷ The surface roughness for each surfaces is presented in **Table 6.1** and a graph of friction coefficient versus surface roughness for the cellulose surfaces is plotted in **Figure 6.4**. The friction coefficient is highest for the symmetric sphere-sphere case, which also

has the highest surface roughness, and the friction coefficient is lowest for the microcrystalline cellulose surface, having the lowest surface roughness.

Table 6.1 Surface roughness friction coefficient and onset of steric repulsion

surface	rms (nm)	rms, flatten (nm)	onset of steric repulsion (nm)	friction coefficient
cellulose sphere	32	10.7	9.1	1.02
spin-coated, neat	10.1	10	13	0.74
spin-coated, annealed	13	9	6.6	0.64
nanocrystalline cellulose	2.1	2.1	18	0.41
silica	0.5	0.3	5	0.18

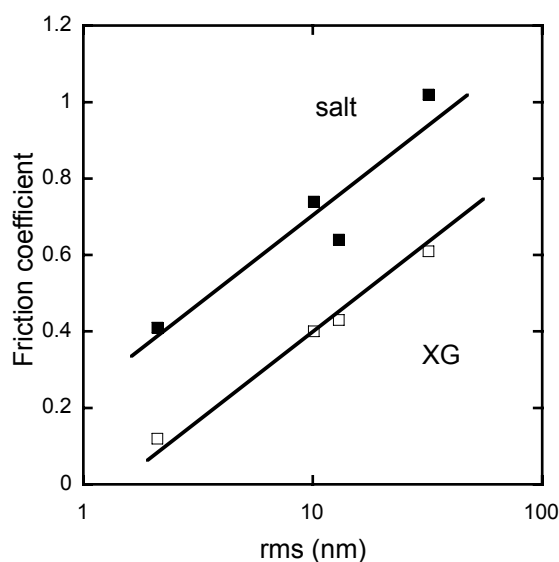


Figure 6.4. Friction coefficient as a function of rms for measurements between a cellulose sphere and another cellulose sphere, an annealed spin-coated cellulose surface, a neat spin-coated cellulose surface and a nanocrystalline cellulose surface immersed in solutions of 0.1mM NaCl (closed squares) and 1 mg/mL xyloglucan, XG, (open squares). The two solid lines, which are drawn to guide the eye, have the same slope.

All surfaces in **Figure 6.4** are cellulose having basically identical surface chemistry, and the only difference between them is the surface roughness, thus it is very clear that the surface roughness has a large impact on the friction coefficient. The open squares show the friction coefficients for the same surfaces with xyloglucan (XG), a friction reducing additive further discussed in section 6.2.1, which changes the

chemistry of the surfaces, whereas the surface roughness presumably remains constant. The friction coefficients in both sets of experiments show identical dependence on surface roughness giving some of the first results showing the effect of roughness at the nanoscopic scale, while the absolute values are determined by the chemistry.

The silica surface is not included in **Figure 6.4** since it has a different chemistry compared to cellulose. The friction coefficient for silica (0.18) is lower than for all of the cellulose surfaces, as seen in **Figure 6.3**, and the surface roughness is also lower than for all of the cellulose surfaces.

The normal forces for silica are shown in **Figure 6.5**. The fitted potential for the silica plate, -25 mV, is rather low for silica, but it agrees well with the cellulose surfaces. The steric repulsion for silica is of shorter range than for all of the cellulose surfaces, as expected due to the different character of silica compared to cellulose. To further investigate the interaction of silica, measurements in symmetric silica systems have also been performed.

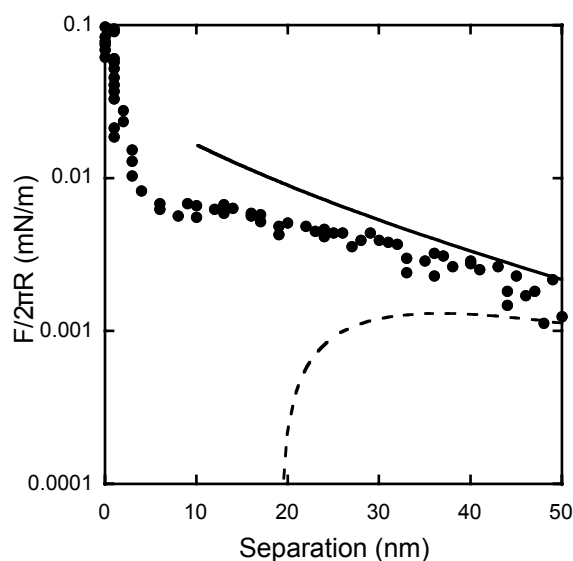


Figure 6.5. Normalized force profiles between a cellulose sphere and a silica plate immersed in a 0.1 mM NaCl solution. The lines are fits of DLVO theory to the data with Debye length 30 nm (calculated value, not a fitting parameter) and Hamaker constant 8×10^{21} J. The solid line represents the constant charge boundary condition, and the dashed line the boundary of constant potential. The fitted surface potential is -8/-25 mV.

6.1.2 Silica

Glass was studied with the MASIF in PAPER I and silica with the AFM in the appendix. **Figure 6.6** shows the normalized force profiles on approach between two glass spheres (open squares) measured at pH 8.5, and between a silica sphere and a silica plate (closed diamonds) at pH 10. The solid lines are fits of DLVO theory to the data, with the boundary condition of constant charge, which return an apparent surface potential, ψ_0 , of -85 mV for the glass surfaces (upper line) and $\psi_0 = -33$ mV for the silica surfaces (lower line). The Debye lengths, κ^{-1} , are 45 nm and 17 nm respectively, which agree well with the pH for each experiment. The magnitude of the surface potentials differs significantly between the two experiments. Glass and silica are not chemically identical; glass consists mainly of silica, but also to 20% of soda (Na_2CO_3), and borosilicate glass as used in the MASIF experiments contains additionally about 5% boric oxide. The surface potential is also critically dependent on the pre-treatment of the surfaces. The glass surfaces were melted in an oxygen-butane flame, providing effective plasma treatment, which increases the number of silanol groups. The silica surfaces were cleaned by acid/base cooking, but not treated with plasma, and thus show much lower surface potential.

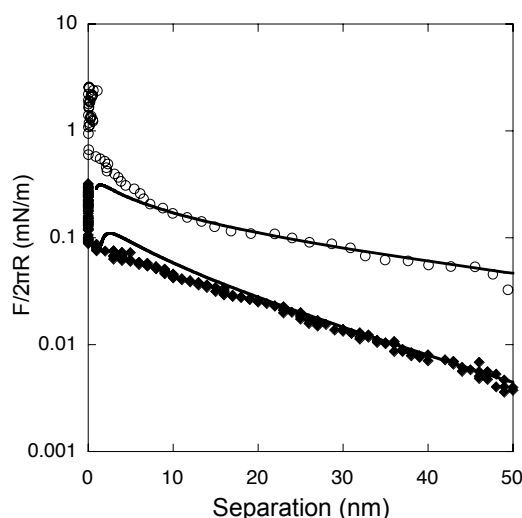


Figure 6.6. Surface forces on approach between two glass spheres immersed in water at pH 8.5, measured with MASIF (open circles, data from PAPER I) and between a silica sphere and a silica plate immersed in water at pH 10, measured with AFM (closed diamonds, data from the appendix). The solid lines are fits of DLVO theory (constant charge boundary conditions) to the data with $\psi_0 = -85$ mV and $\kappa^{-1} = 45$ nm for the glass surfaces, and $\psi_0 = 33$ mV and $\kappa^{-1} = 17$ nm for the silica surfaces.

The steric repulsion is more pronounced for the higher surface potential, though of shorter range than for cellulose. It is typical for glass and silica surfaces in aqueous

solutions and has been ascribed to hydration forces,^{2,20} as also discussed in section 2.4.1.

6.1.3 Interactions in air

So far the measurements have been concerned with interactions in liquid, however interactions have also been measured between both silica and cellulose in air, with a view to understanding the role of capillary condensation on adhesion, and also its affect on the lateral strength of a joint or contact (which we can infer from frictional measurements).

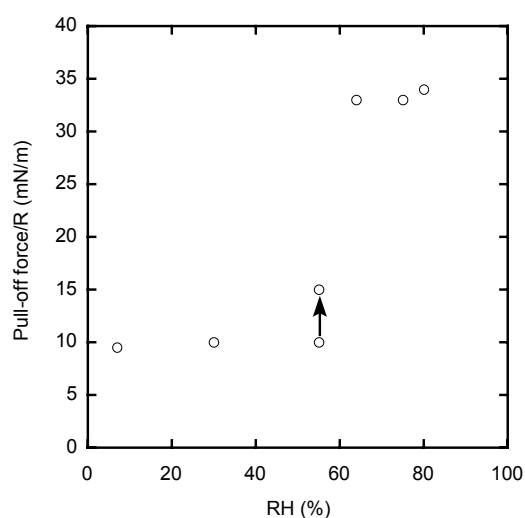


Figure 6.7. Adhesion as function of relative Humidity between two cellulose particles. The arrow indicates changes with increased conditioning time. At 55% RH the adhesion increased somewhat after a friction measurement had been performed.

The results for the adhesion as a function of relative humidity between two cellulose surfaces conditioned overnight are shown in **Figure 6.7**. At lower humidities the adhesion is rather low, but it increases significantly above a threshold value which is around 55% relative humidity. While the theory for adhesion between two smooth surfaces predicts an adhesion independent of the relative humidity,^{15,69} the observation of an adhesion threshold has been made earlier for non-ideal surfaces.^{27,70,71} In this case it is held that at lower humidities the Kelvin radius of the condensate is smaller than the surface asperities and thus any condensates can occur only between contacting asperities. At higher humidities the Kelvin radius exceeds the roughness and the contact is flooded, leading to a considerably enhanced adhesion.

The friction force also increases above the threshold, whereas the friction coefficient decreases. The friction traces for cellulose surfaces for a few humidities are shown in **Figure 6.8**. Importantly, the same frictional force was measured again at low humidities after the measurements equilibrated at the high RH indicating that the state of the surfaces and the water condensate is reversible with long enough equilibration. The friction is approximately linear with increasing applied load, as predicted by Amontons' law, but does not go through the origin. From zero load (non contact) the friction force jumps straight to the intercept value. This indicates that there is an adhesive contact between the surfaces, and the intersect of the projected continuation of the line of best fit with the Load axis is a measure of the adhesion between the surfaces. Thus, the frictional force depends both on the externally applied load, plus an additional "intrinsic" load due to the adhesion caused by the capillary condensate. However, the water also has a lubricating effect which reduces the friction coefficient.

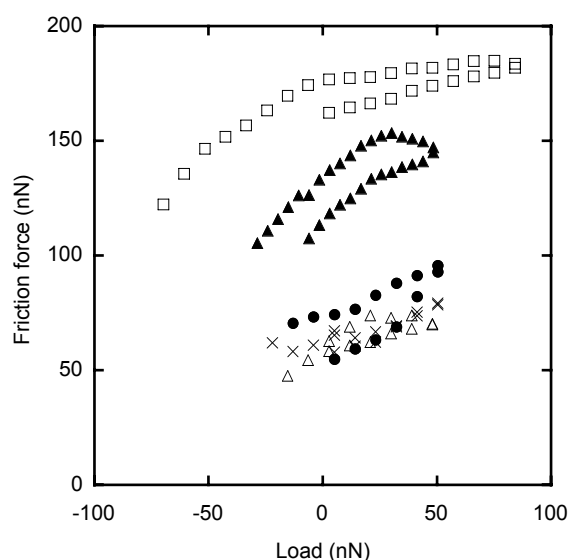


Figure 6.8. Friction-load traces between two cellulose spheres performed at 7% RH (open triangles), 55% (filled circles), 80% (open squares), 55% after being at higher humidity (filled triangles), and 7% after being at higher humidities (crosses). The friction coefficients obtained from the linear slopes yielded: $\mu_{7\%} = 0.26$, $\mu_{55\%} = 0.51$, $\mu_{80\%} = 0.25$, $\mu_{55\% \text{ after higher humidity}} = 0.64$ and $\mu_{7\% \text{ after higher humidity}} = 0.22$.

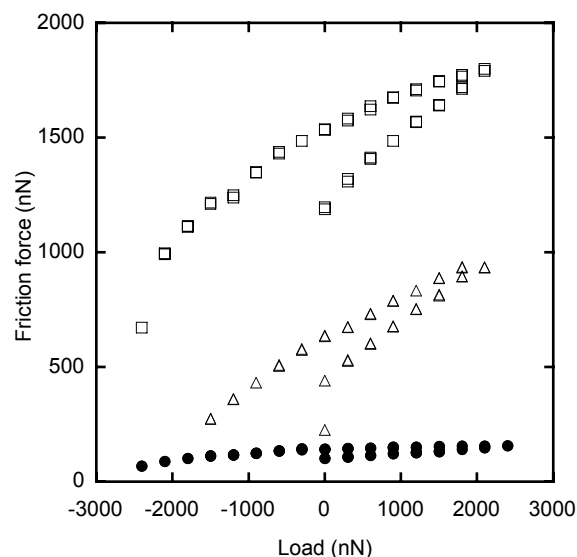


Figure 6.9. Friction behaviour of a glass probe sliding on silica (squares) and hydrophobized silica (triangles) and mica (circles) in ambient conditions (64% RH, 22°C) after preconditioning the system for 24 hours at 65-70% RH. The friction coefficients obtained from the linear slopes yielded: $\mu_{\text{mica}} = 0.02$, $\mu_{\text{silica hydrophilic}} = 0.13$, $\mu_{\text{silica hydrophobic}} = 0.15$.

In **Figure 6.9** friction–load relationships are displayed for the case of a silica colloidal probe interacting with a hydrophilic silica surface, a hydrophobized silica surface and a mica surface after 24 hour conditioning at high relative humidity. The absolute values of the friction are very different for the three curves with the atomically smooth mica surface having the lowest friction. The highest friction is observed for the silica-silica case, which is also the case with the highest surface roughness, so this is ascribed to a mechanical interlock mechanism since both surfaces have approximately the same roughness. That friction increases with increasing surface roughness has also been observed for cellulose (**Figure 6.4**) Often it is difficult to compare friction values for different substrates directly since the adhesion values can vary significantly, which effectively alters the applied load. In this case the adhesion values are the same (because the capillary condensate dimensions are essentially the same) so direct comparison is possible, and the difference can consequently be ascribed to the roughness. The values of the adhesion are much lower for cellulose than observed for mica and silica surfaces, even above the threshold, probably revealing that the roughness of cellulose is too large for a full condensate to form.

Turning now to compare cellulose and silica, which have reminiscent friction traces above the threshold, it is obvious that both adhesion and friction forces are much higher for silica than for cellulose. This difference is a result of the fact that a

complete capillary condensate is formed for silica, but not for cellulose. Earlier measurements of adhesion of silica²⁷ showed much lower adhesion. The large adhesion in **Figure 6.9** is a result of the presence of a mature condensate that is able to completely flood the contact zone since the Kelvin radius is larger than the roughness of the contact. In the case of cellulose, which is also hydrophilic, although less so, the roughness is much larger and thus complete flooding is not possible – the adhesion values in **Figure 6.7** and inferred from the negative loads of **Figure 6.8** are therefore much lower. There is a threshold and thus considerable flooding – this reflects that there is roughness on various scales for the cellulose.

Cellulose would be expected to have larger friction than silica due to the larger surface roughness, and this is indeed the case in friction coefficient terms – the friction coefficient is higher for cellulose (0.35) than for silica (0.15) however the larger adhesion for silica increases the magnitude of the friction forces for silica significantly.

It is interesting to note that while both adhesion and friction increase for the model cellulose surfaces found here, paper strength actually reduces at higher humidities (corresponding to above the threshold). Clearly the strength of paper cannot be simply treated in terms of the individual adhesional components at the contacts. The effect of the capillary condensation will be to partially solubilise and hydrate the polymeric material at the fibre joints (for example strength additives as well as natural wood polymers), as well as to swell the cellulose, all of which may well have the effect of actually weakening the joint. Paper strength, for example measured through the so called “burst strength” is usually considered in terms of tensile strength and stretch. Different regimes have been identified but above 55% RH, the decrease in tensile strength is greater than the increase in stretch, and bursting strength decreases continuously.⁷²⁻⁷⁴ It seems likely from these measurements that the mechanism for water uptake which causes the strength failure, is driven by the growth of capillary condensates, which may even act as a reservoir for absorption.

6.2 Surface modification

6.2.1 Xyloglucan

Xyloglucan is a polysaccharide found in the plant cell wall in which it is generally believed to cross-link load bearing cellulose microfibrills and affect wall mechanical properties.⁷⁵⁻⁷⁹ Indeed, many studies have shown that xyloglucan adsorbs strongly to cellulose⁸⁰⁻⁸⁴ and, recently, this specific interaction has been harnessed in the development of a new versatile method to functionalise cellulosic surfaces.^{85,86} Attempts have also been made to add xyloglucan to the pulp before paper sheets are formed, with an approximately 20-30% increase in the tensile strength of paper as a result.^{13,14} Another benefit of xyloglucan addition to pulp is that the paper becomes smoother as a result of better paper formation.¹³ It has been speculated that the increased paper strength is a result of stronger cellulose-cellulose joints, and that the paper formation is improved by reduced friction between the fibres.¹³

Figure 6.10 shows the normalized force-distance profiles between two cellulose spheres in solutions of 0.1 mM NaCl, 1 mg/mL xyloglucan (XG) and 0.1 mM NaCl after rinsing away any non-adsorbed XG, on a logarithmic scale. The effect of XG on the interaction profile is clearly evident; there is significant increase in the range and magnitude of the repulsive force upon addition of XG, and it does not change appreciably after rinsing. The surface potential increases and after rinsing remains unchanged, indicating that the XG is irreversibly adsorbed. The highly substituted, parts of XG are thought not to bind to cellulose, but instead form loops and make the XG more bulky. The presence of unbound groups probably renders the polymer more mobile and increases the probability of chain end detachment and reattachment to an opposing surface, thereby facilitating cross-linking between cellulose fibres.⁸² Such loops increase the repulsion on approach, and since any charged groups extend out into the solution it is likely that a very small fraction of charges has a relatively large impact on the measured surface potential.

The range of the electrosteric repulsion also becomes longer when the XG solution is added, and it decreases only slightly in range after rinsing, suggesting that only a small fraction of the XG is so loosely adsorbed that it desorbs on dilution. Besides the XG molecules having higher surface charge than cellulose, it is likely that XG chains, being water-soluble, extend further out in the solution than cellulose chains, which are insoluble in water, thereby increasing the electrosteric repulsion.

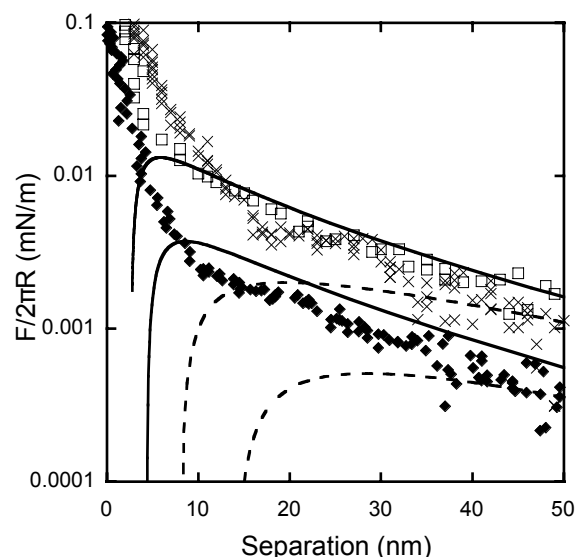


Figure 6.10. Force curves on approach between two cellulose spheres in solutions of 0.1 mM NaCl (filled diamonds), 1 mg/mL XG (open squares), and after rinsing with 0.1 mM NaCl (crosses) plotted on a logarithmic scale. The lines are fits of DLVO theory to the data, with surface potential -8 mV for the lower set of lines, and -13 mV for the upper set of line. The solid lines represent the constant charge boundary condition, and the dashed lines represent the constant potential boundary condition. The Debye length was 30 nm for both fits (calculated value, not a fitting parameter).

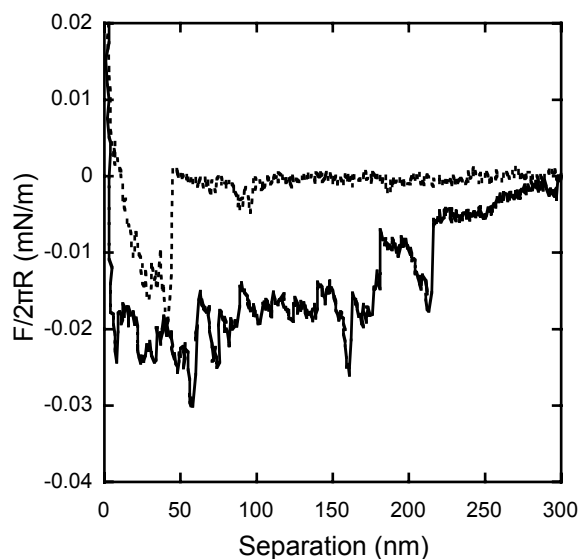


Figure 6.11. Force curves on retraction between two cellulose spheres in a solutions of 1 mg/mL XG for two different times in contact. The dotted time represents 1 second in contact, and the solid line 100 seconds.

The forces on separation in 1 mg/mL XG are presented in **Figure 6.11**. The dashed curve represents the interaction in XG at a rate of 0.2 $\mu\text{m/s}$, and the solid curve

represents the interaction under the same conditions but with 100 s prolonged time in contact. The adhesion is larger in the presence of XG compared to the bare cellulose surfaces, and the adhesion is very sensitive to the time in contact. In the presence of XG the surfaces jump apart to a position well beyond the range of the surface force. The adhesion is a result of the specific binding between cellulose and XG as indicated by the saw-tooth pattern which is typical for the pull-off of individual chains, commonly seen between surfaces with adsorbed polymers.^{87,88} The interaction profile is very irregular, indicating that a large number of cellulose-XG bonds with different contour lengths are present.

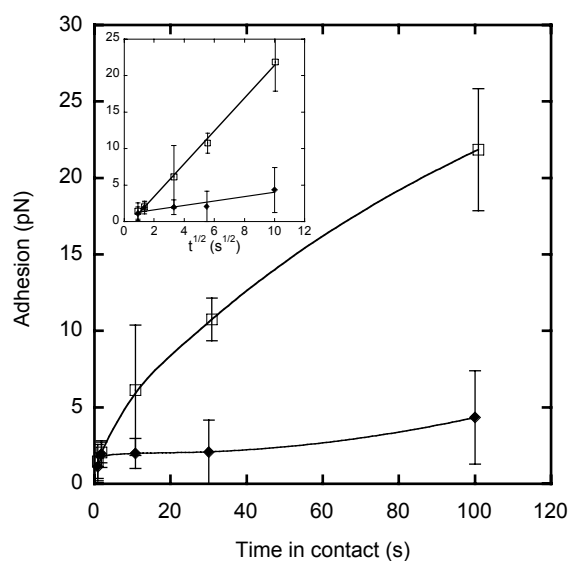


Figure 6.12. Work of adhesion as a function of contact time for two cellulose spheres in solutions of 0.1 mM NaCl (closed diamonds) and 1 mg/mL XG (open squares). The inset shows the adhesion as a function of $t^{1/2}$. The lines are added to guide the eye.

Figure 6.12 shows that the work required to separate the surfaces in XG solutions is linearly dependent on the square root of the time in contact, suggesting that the adhesion is controlled by a diffusion process.^{89,90} This is consistent with parts of XG chains diffusing to the opposing cellulose surface and creating cross-links. The time-dependent adhesion, together with its clear saw-tooth pattern in **Figure 6.11**, provide strong evidence for bridging of XG between cellulose surfaces.

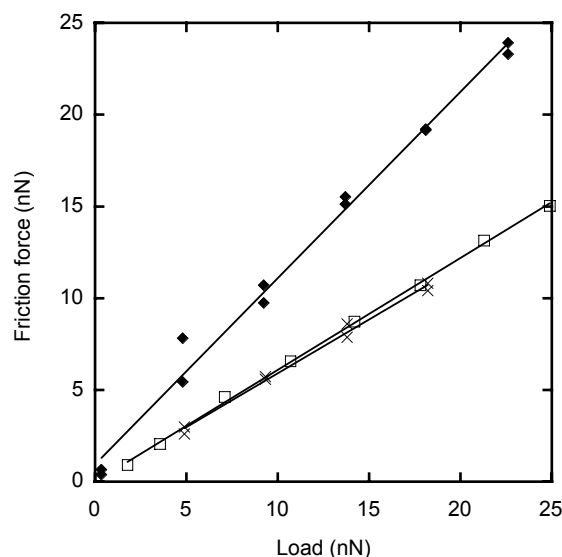


Figure 6.13. Friction force as a function of applied load for two cellulose spheres in solutions of 0.1 mM NaCl (closed diamonds), 1 mg/mL XG (open squares), and 0.1 mM NaCl after rinsing (crosses). The solid lines represent the friction coefficients, which are $\mu = 1.02$ in NaCl, $\mu = 0.61$ in XG and $\mu = 0.59$ after rinsing.

In **Figure 6.13** the lateral friction as a function of applied load is shown for a cellulose sphere sliding against another sphere, immersed in 0.1 mM NaCl in the presence and absence of 1 mg/mL XG. The friction is zero for zero applied load for all measurements and the friction follows Amontons' law (Equation 2.12). The friction coefficient is highest for the bare cellulose, $\mu = 1.02$, and it decreases by almost a factor 2 in the presence of XG, $\mu = 0.61$. The friction coefficient does not change significantly after rinsing, providing further evidence that the XG molecules are not rinsed away, and that it is the bound XG and not the loosely bound that reduces the friction.

The question remains, however, as to the mechanism of the friction reduction. Increased adhesion is generally associated with increased friction^{26,91-94} and the system becomes more adhesive in the presence of XG. Now, the adhesion is only manifested after the surfaces have been brought into close contact and water has been expelled from the contact zone, and in the presence of XG, the adhesion increases significantly with increasing time in contact. As the surfaces slide past each other the XG molecules do not have time to bind to the opposing surface since the sliding rate is fast compared to the time scales required for bridging. If bridging were able to occur during the time scale of the measurements then it would indeed increase the friction force.⁹⁵

On approach, however, there is repulsion, which increases in the presence of XG, and an increased repulsion between the surfaces is generally associated with a decrease of the measured friction.⁹⁶ The XG molecules effectively create a boundary lubricating layer, which imparts a steep repulsive force. It is also likely that the XG molecules create a well defined slipping plane between the cellulose surfaces.

Surface force measurements clearly confirm that xyloglucan adsorbs irreversibly to cellulose. An important effect of the xyloglucan adsorption is that the very small adhesion between cellulose surfaces in water is significantly increased due to the bridging and formation of specific bonds of xyloglucan to both surfaces. This provides a mechanistic explanation for the recent observation that the tensile strength of paper increases about 20-30 % by addition of xyloglucan.^{13,14}

These results also show that the adsorbed xyloglucan significantly reduces friction giving support to the view that the improved formation is indeed due to beneficial friction properties imparted by xyloglucan as speculated by Christiernin *et al.*¹³. It would appear that xyloglucan is thus in many ways an ideal additive since it combines apparently incompatible characteristics. The friction reduction is associated with the increased *repulsion* between the cellulose surfaces whereas the strength is imparted by increased *adhesion* (attractive). The apparent conundrum is resolved by the fact that the bridging forces have a much longer relaxation time than sliding residence times, and the adhesion is only activated after the surfaces are forced into contact, which in the case of paper occurs as capillary forces drive the fibres into intimate contact during drying.

6.2.2 Surfactants

Cationic surfactants readily adsorb on negatively charged surfaces, such as cellulose and glass, and a schematic of surfactant adsorption is shown in **Figure 6.14**. Industrially, cationic surfactants are used as softeners and lubricating agents, and mixtures of cationic and non-ionic surfactants are for example used to control the friction during manufacturing of viscose fibres. In order to reveal the effect of surfactant aggregates on surface interactions normal and friction forces in surfactant solutions have been studied by means of MASIF and AFM. Chronologically, the MASIF measurements were performed first, before the capacity to measure friction with AFM had been developed in house, which explains the two experimental sets.

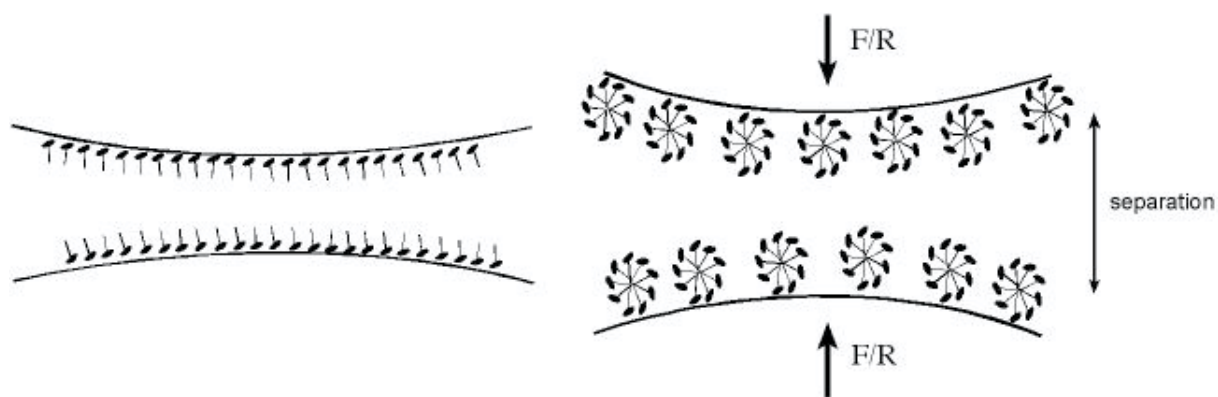


Figure 6.14. A schematic of surfactant adsorption on oppositely charged (or uncharged hydrophilic) surfaces. Left image: low concentrations, below cmc. Right image: Above cmc. For further discussion of surfactant adsorption see section 3.2 and PAPER I.

Addition of low concentrations of cationic surfactant removes the hydration repulsion as the surfactants adsorb to the glass surface with the hydrocarbon tails towards the solution. The surfaces jump into adhesive contact at small surface separations as seen in **Figure 6.15**, closed symbols, which depict the interaction force in 0.5 mM TTAB. On separation the surfaces are adhesive, as also observed previously.^{29,97,98} As the surfactant concentration is increased the adsorbed layer becomes denser which increases the adhesion in accordance with proximal adsorption theory and Equation 3.1. The adhesion reaches its maximum just below the cmc. At higher concentrations surfactant aggregates form at the surfaces, as also shown by long ranged double layer forces and additional short range force barriers (**Figure 6.15**, squares and crosses). The barrier force, F_b , is the force required to push out the surfactant aggregates from the contact region. The two solid lines are fits of DLVO theory to the 3.5 mM TTAB data with boundary conditions of constant charge (upper) and constant potential (lower), returning an apparent surface potential of 55 mV and a Debye length of 5.1 nm, which agrees well with the TTAB concentration of 3.5 mM assuming full dissociation of the surfactants and the counter-ions. Due to the presence of the surfactant aggregates, the plane of charge had to be moved and is assumed to be located 4 nm from hard wall contact. The data clearly display that the glass surface is neutralized by the cationic surfactants, and subsequently recharged, since the double layer repulsion is absent at 0.5 mM (neutral surfaces) and reappears above this concentration.

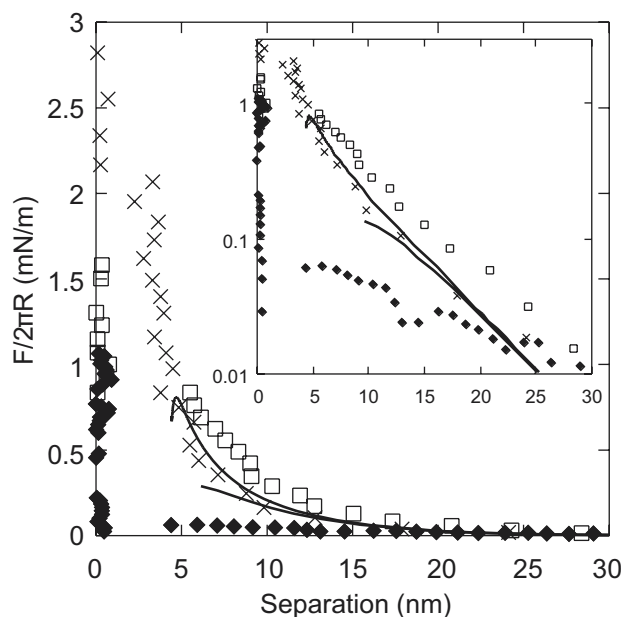


Figure 6.15. Surface forces measured with the MASIF on approach between two glass spheres immersed in TTAB solutions (closed diamonds, 0.5 mM; squares, 2 mM; crosses, 3.5 mM). The inset shows the force curves on a logarithmic scale. The solid lines show a fit of DLVO theory to the 3.5 mM TTAB data with $\psi_0 = 55$ mV and $\kappa^{-1} = 5.1$ nm.

In both experiments the relation between surface potential and the barrier force in the TTAB solution at *cmc* was identical. The qualitative agreement between the two sets of experiments is reassuring, however the quantitative difference underlines the importance of the pre-treatment for the surface properties of silica.

After the barrier has been overcome the surfaces are adhesive on separation, whereas there is no adhesion at all between unruptured aggregates. The pull-off force for the MASIF experiment **Figure 6.16** increases with increasing TTAB concentration as a hydrophobic layer is built up on the surfaces. However, the adhesion reaches a maximum, and as the surfactant aggregates are formed at higher surfactant concentrations the adhesion is reduced^{97,98}. The same trend, though with relatively lower adhesion values, was observed in the AFM experiment.

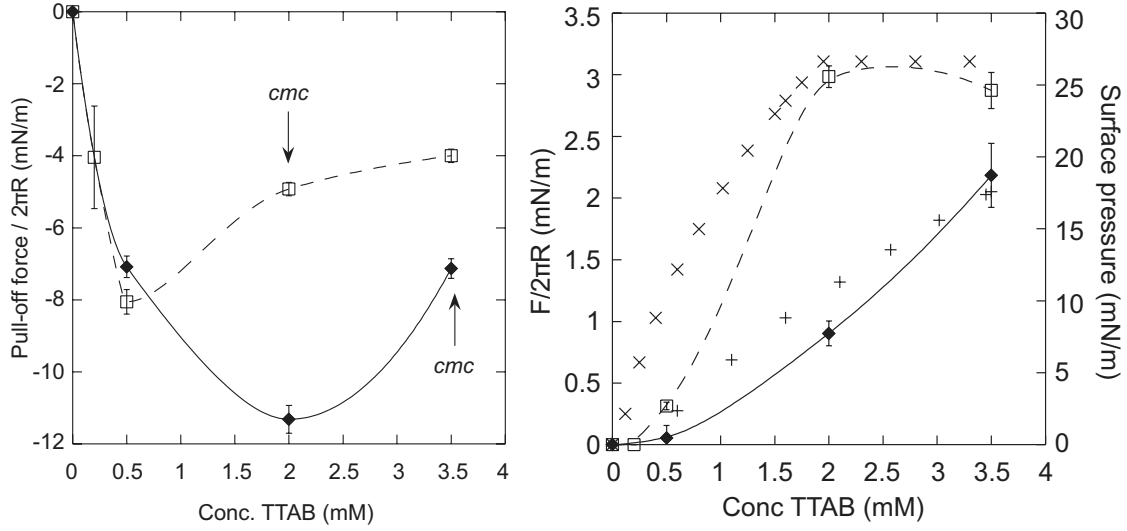


Figure 6.16. Left panel: Pull-off force as a function of TTAB concentration for solutions with 10 mM added NaBr (open squares and dashed line) and without added salt (closed diamonds and solid line). The lines are drawn to guide the eye.

Right panel: Barrier force as a function of TTAB concentration with 10 mM added NaBr (open squares and dashed line) and without added salt (closed diamonds and solid line), and surface pressure, calculated by Equation 6.1, as a function of TTAB concentration with 10 mM added NaBr (crosses) and without added salt (plus signs).

The values of the surface pressure for TTAB on silica, plotted in **Figure 6.16**, have been calculated from adsorption data measured by Wängnerud *et al.*^{99,100} using

$$\pi = RT \int_0^{c_b} \Gamma_{ij} d \ln c \quad (6.1)$$

which is valid for an ideal case below the *cmc* since the chemical potential then is proportional to $\ln(c)$. The force barrier and the surface pressure of Wängnerud clearly follow the same trend; however, the magnitudes differ by a factor of roughly 2π . The barrier force, when present, thus seems to be a useful measure of the adsorbed amount. The small discrepancy between the surface pressure and the force barrier at low concentrations of TTAB is attributed to the absence of barrier force when the surfaces jump into adhesive contact, even though there indeed is a surface pressure due to the adsorption. Further, the surface pressure describes all the surfactant aggregates on one single surface, whereas the barrier force is exerted by the surfactants that are pushed out when *two* surfaces come into contact. For comparison, it has been shown that the surface pressure of a monolayer of polymer on a hydrophobic surface corresponds to half the barrier force of two such surfaces at monolayer-monolayer contact^{101,102}.

The friction between a silica sphere and a silica plate in TTAB solutions vary strongly with TTAB concentration due to the action of the adsorbed surfactants as is shown in **Figure 6.17**. The friction force in water, which was briefly discussed in connection to the cellulose silica data in section 6.1.1, is linearly dependent on the applied load and follows Amontons' law as also seen for cellulose surfaces in water. The friction force increases for the 0.1 mM TTAB solution compared to water due to the increased adhesion, and the friction force is substantial at zero applied load. For the 1 mM TTAB solution the adhesion is further increased, but the friction coefficient here decreases as a result of the lubricating effect of the surfactant. At 4 mM TTAB (above the cmc) the friction is initially very low, and when the barrier force at about 10 nN is overcome the friction force increases in a "step-wise" manner, however there is still a sufficient amount of surfactants left in contact for the friction coefficient to continue to be low. The low friction above the *cmc* is probably connected to the formation of a well defined shear plane and a stiff force barrier which takes up the load and smoothens the surface roughness.

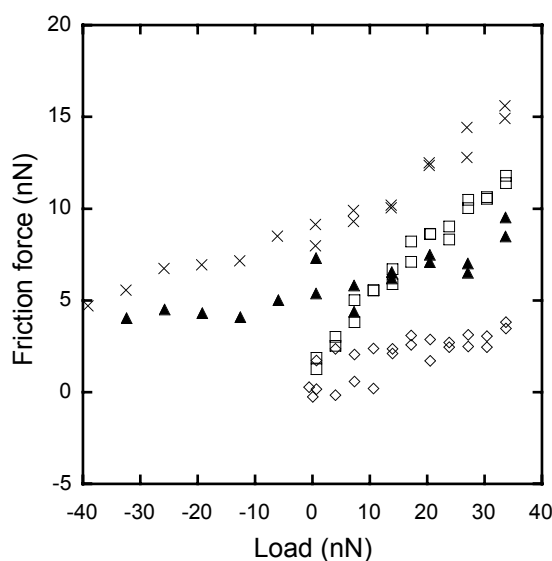


Figure 6.17. Friction versus load data between a silica sphere and a silica plate in water (squares) and solutions of TTAB at 0.1 mM (crosses), 1 mM (triangles) and 4 mM (diamonds). The friction coefficients obtained from the linear slopes yielded: $\mu_{\text{water}} = 0.30$, $\mu_{0.1\text{mM}} = 0.14$, $\mu_{1\text{mM}} = 0.07$, $\mu_{4\text{mM}} = 0.04$.

Nonionic surfactants have a lower driving force to adsorb at negatively charged surfaces than cationic surfactants, however the cmc is lower (given that the two surfactants have equally long hydrocarbon chains) since there are less repulsion between the headgroups, which for cationic surfactants hinders aggregation. Thus, in a mixture of cationic and non-ionic surfactants, the cationic surfactant work as anchors on the surface where they adsorb at very low concentrations. The non-ionic

surfactants may then co-adsorb such that surface aggregates are formed at concentrations much below the cmc for the cationic surfactant. This adsorption is displayed by the existence of a force barrier, once the surfactant concentration exceeds cmc of the mixture, which is very low compared to the cationic surfactant.

Figure 6.18 shows friction – load data between a silica sphere and a silica plate in water (squares) and increasing concentrations of a 1:4 TTAB - $C_{14}E_6$ mixture. At a total surfactant concentration of 0.01 mM (crosses), which is below the cmc for the mixture, the friction force increases compared to water, due to an increased adhesion caused by a minor adsorption of TTAB. However, already at 0.1 mM (triangles), the friction is almost nonexistent, due to the formation of surfactant aggregates on the surface. In fact, the friction occasionally looks negative, but this is of course impossible (unless the friction is defined as a vector, which is not the case here), instead the negative friction reflects that the friction is lower than the resolution of the instrument.

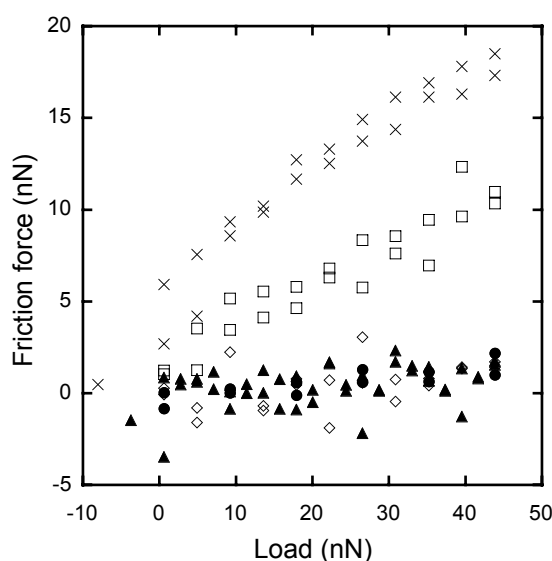


Figure 6.18. Friction versus load data between a silica sphere and a silica plate in water (squares) and solutions of TTAB- $C_{14}E_6$ 1:4 mixtures at total surfactant concentrations being 0.01 mM (crosses), 0.1 mM (triangles), 1 mM (diamonds) and 20 mM (circles). The friction coefficients obtained from the linear slopes yielded: $\mu_{\text{water}} = 0.25$, $\mu_{0.01\text{mM}} = 0.33$, $\mu_{0.1\text{mM}} = 0.03$, $\mu_{1\text{mM}} = 0.04$, $\mu_{4\text{mM}} = 0.04$.

The friction is critically dependent on the concentration, as well as the composition, of the surfactant solution.

6.3 Technique development

The AFM has traditionally been employed for lateral friction measurements, in which the cantilever scans the surface at increasing loads while the response in the lateral detector is recorded as described in section 4.5. The quantification of the results is, however, nontrivial. The calibration methods for lateral force constants that have been proposed over the years depends either on an *ex situ* calibration,⁴⁹⁻⁵² or on calculations of material properties.⁵³⁻⁵⁷ In addition, many older AFMs are specifically designed for normal force measurements and have no lateral capacity. Thus, it would be useful to have a technique for obtaining friction from normal force measurements, particularly if the calibration could be performed *in situ*. Such a method is the focus of PAPER V and briefly presented here.

The method exploits the fact that AFM cantilevers sit at an angle of about 10° to the horizontal. This angle causes the probe to slide horizontally over the substrate as a force measurement is performed, and the consequent friction force causes a bend in the cantilever in addition to that due to the normal force, as illustrated in **Figure 6.19**.

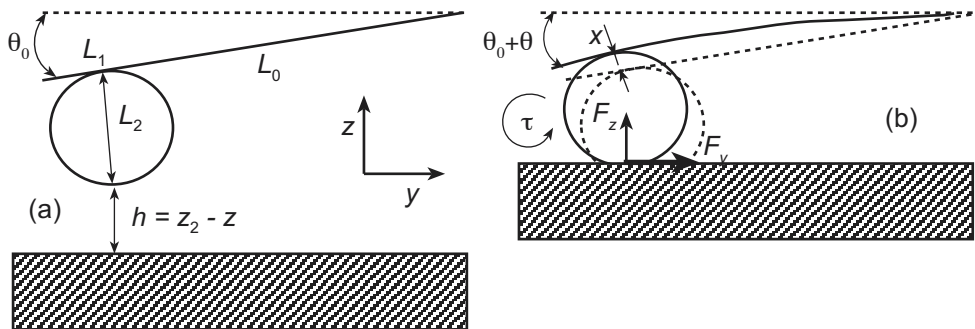


Figure 6.19. A model of the AFM. The lower surface is mounted on a piezo-translator and the upper surface is a colloidal probe of length L_2 attached at a point $L_1 + L_0$ from the fixed base of the cantilever, where L_0 is the length of the flexible part of the cantilever, and L_1 is the extent of the glue attaching the probe. Usually, $L_0 \gg L_2 \gg L_1$. The cantilever makes an angle θ_0 to the horizontal. The deflection of the end of the cantilever is x and the angular deflection is θ ; the actual angle of the tip is $\theta_0 + \theta$; negative values correspond to down. (The deflection is greatly exaggerated in the figure; in all cases $x \ll L_0$ and $\theta \ll \theta_0$.) The vertical position of the tip of the cantilever probe is z_2 and its horizontal position in the axial direction is y_2 . (a) Out of contact. (b) In contact, with the substrate moving up and the probe sliding to the left.

Bending due to friction in a normal force run is barely detectable for an ordinary AFM tip, whereas, for larger probes, the deflection due to axial friction becomes more pronounced, and while using large probes for normal force measurements the

deflection due to axial friction is of rather significant magnitude. For large probes the associated horizontal sliding may actually be used to measure the friction.

The deflection due to axial friction is manifested in the slopes of the constant compliance lines in the raw data from the AFM, causing the slopes to become non-parallel. An example of AFM raw data with different amount of axial deflection is shown in **Figure 6.20**.

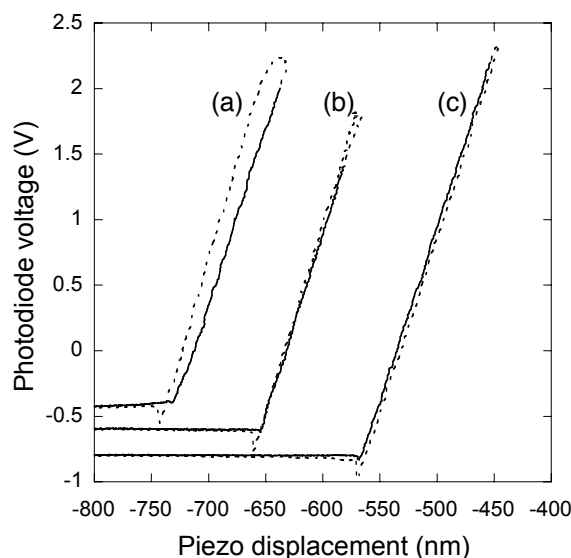


Figure 6.20. Cantilever deflection in terms of the photo-diode voltage as a function of piezo z-position, for three cantilevers with different probe diameters: (a) 36 μm , (b) 16 μm and (c) without probe. Solid lines refer to loading and dashed lines to unloading traces. All cases were measured in 0.1 mM NaCl solutions, with scan size 1 μm and scan rate 1 Hz.

The horizontal sliding, which is illustrated in **Figure 6.21**, is significant and increases with increasing probe size. The data in **Figure 6.21** were obtained using Equation (15) of PAPER V. It has not always been fully appreciated just how much axial sliding of the cantilever on the substrate occurs during a normal force measurement. **Figure 6.21** shows that the horizontal motion can be of the order of 50-100% of the vertical motion of the piezo-drive in contact.

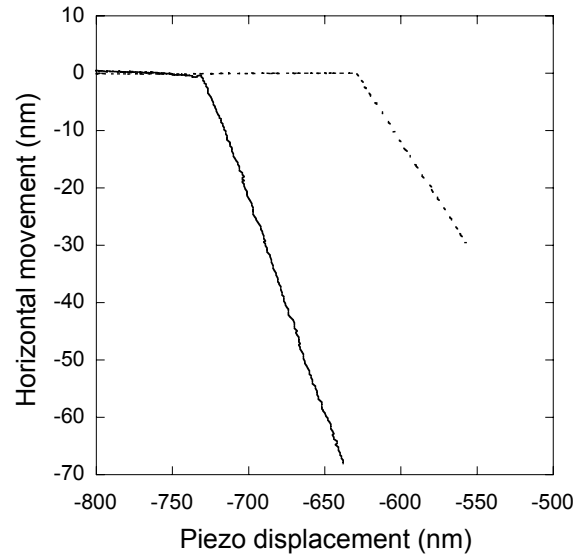


Figure 6.21. Horizontal position, y_2 , of the cantilever probe as a function of piezo-drive z-position (same cases as in Fig. 2). The solid line represents the 36 μm probe and the dashed line represents the 16 μm probe.

Frictional data was extracted from the normal force run following Equations 18 and 19 of PAPER V, which specify the surface force and the friction force in the contact regime. Figure 5 shows the friction versus load data for the two probes. The solid line shows the friction force during loading (inward trace), and the dashed line shows the unloading (outward) trace. The friction reaches its maximum value just before the piezo changes direction, which causes the probe to roll, and on unloading the friction becomes negative due to the change in direction of the probe on the substrate. (Of course the friction force is a vector and as such it has a sign. Conventionally, however, only the magnitude of the friction force is reported.) The nature of the friction and its dependence upon load during the rolling of the probe following the change in piezo-direction is obviously qualitatively different to the friction that occurs during the steady sliding of the probe along the substrate. It is only from the latter that friction coefficients are extracted.

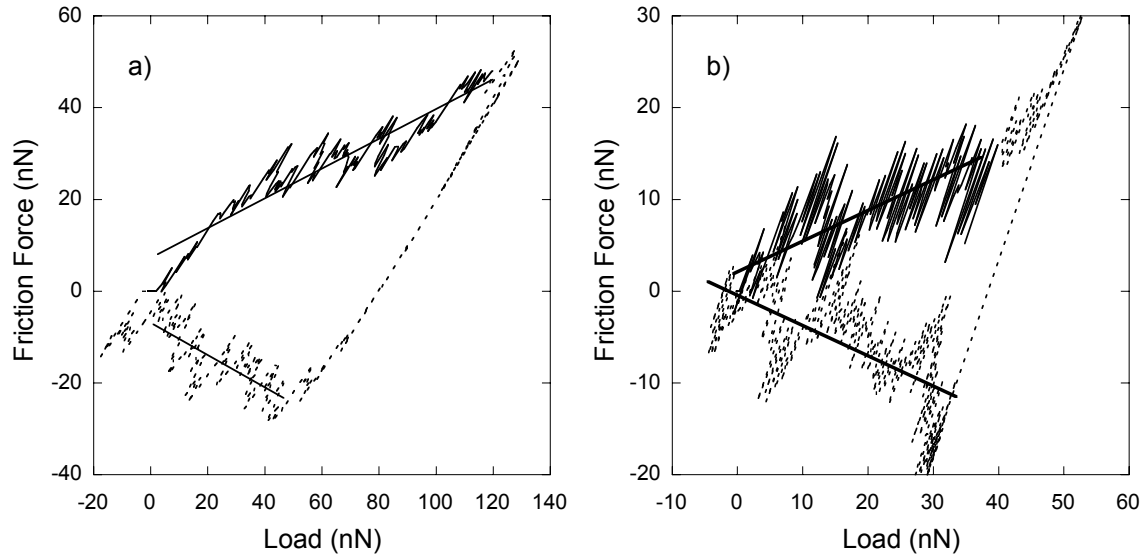


Figure 6.22. Friction force as a function of normal applied load during loading (solid lines) and unloading (dashed lines). (a) The probe diameter is $36\ \mu\text{m}$, the z-speed is $1.8\ \mu\text{m s}^{-1}$ and the horizontal speed is $1.4\ \mu\text{m s}^{-1}$, (b) $16\ \mu\text{m}$, $5.4\ \mu\text{m s}^{-1}$ and $2.1\ \mu\text{m s}^{-1}$. Lines of best fit are $F_y = 0.34 (F_z + 18.2\ \text{nN})$ and $F_y = -0.34 (F_z + 20.9\ \text{nN})$ for (a), and $F_y = 0.33 (F_z + 6.4\ \text{nN})$ and $F_y = -0.33 (F_z + 1.2\ \text{nN})$ for (b).

A comparison between the lateral and axial methods are shown in **Figure 6.23**. The lateral measurements were performed immediately after each of the respective axial measurements, in the same cell, and with the same AFM set-up, at a speed of $2\ \mu\text{m s}^{-1}$. It may be seen that there is excellent agreement between the lateral and the axial methods. It should be pointed out that the points in the lateral force measurement are each the average of 20 friction loops, each of which is based on several hundred points of sliding data. The axial friction on the other hand is extracted from a single constant compliance curve and it is thus to be expected that there is a little more noise associated with that measurement!

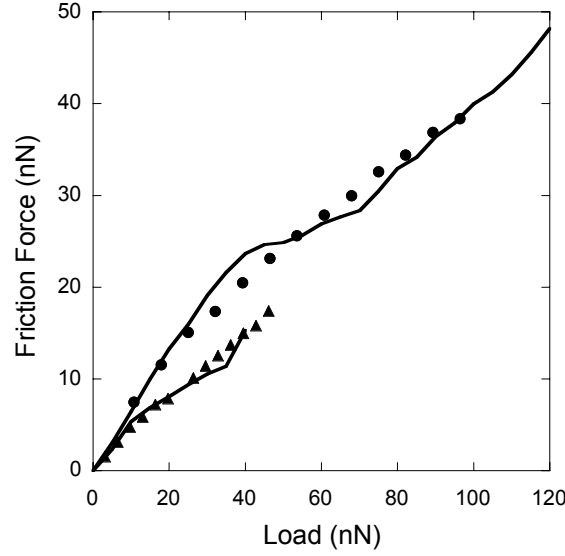


Figure 6.23. Friction force as a function of applied load. The circles represent the lateral friction force measured for probe size 36 μm , and the triangles probe size 16 μm (each averaged over 20 loops). The solid curves are smoothed and averaged loading data from **Figure 6.22** (each averaged over five traces). Only loading traces are shown. Lines of best fits (not shown) are for the lateral method $F_y = 0.34 (F_z + 19.7 \text{ nN})$ and $F_y = 0.34 (F_z + 4.1 \text{ nN})$ for the large and small probe respectively, and for the axial method $F_y = 0.34 (F_z + 17.3 \text{ nN})$ and $F_y = 0.34 (F_z + 2.9 \text{ nN})$ respectively.

The new axial friction method proposed in PAPER V has several advantages. It only requires the bending spring constant of the cantilever that is used in ordinary force measurements, and this is obtained by standard calibration methods. It does not require the twist or torsional spring constant that is problematic to obtain. Also, it does not require calibration of the lateral photo-diode response, which again creates problems for lateral friction methods.

7 Concluding remarks

The surface potential, steric repulsion and adhesion obtained for four different cellulose surfaces vary slightly between the cellulose substrates and depend for example on the properties of the pulp that the cellulose is regenerated from. In addition, the surface roughness differs between the cellulose surfaces, and increasing surface roughness has been shown to increase the measured friction. With continued research and development of model cellulose surfaces, I am convinced that the cellulose model surfaces can be tailored to have almost identical properties as the cellulose fibre one would like to mimic which will allow an exciting combination of fundamental and applied research.

In the presence of xyloglucan the friction of cellulose decreases compared to water, and the same dependence on surface roughness is seen. At the same time xyloglucan increases the adhesion between cellulose surfaces and these two apparently incompatible characteristics provide a mechanistic explanation for the recent observations that both the paper strength and the paper formation are improved by addition of xyloglucan to the pulp.^{13,14} The specific affinity between xyloglucan and cellulose can also be used for anchoring of enzymatically modified xg, opening for a wide range of surface modifications.

Measurements in air show a clear threshold in both friction and adhesion at about 60% relative humidity, which is attributed to the formation of large capillary condensates. The threshold correlates well with the onset of weakening for paper, implying that water deposited on the surface of fibres via capillary condensates is ultimately responsible for this phenomenon. Surface chemistry affects friction significantly but on this roughness scale the net friction is determined by the magnitude of the capillary adhesion, rather than by specific surface chemical effects on the mechanisms of friction. However, the surface roughness is found to be important for the friction coefficient, confirming the finding for cellulose in water.

A clear relationship is observed between the barrier force and the adsorbed amount for cationic surfactant systems. In mixtures of cationic and non-ionic surfactants synergistic effects are seen in the adsorption, giving barrier forces at much lower surfactant concentrations than for the pure cationic surfactant. The existence of a force barrier reduces the friction significantly, and the friction can thus be controlled by tuning surfactant concentration and composition.

Finally, the new axial friction method proposed here has several advantages over the lateral method. Friction data are obtained during the normal force measurement and the friction coefficient is obtained directly from the slopes of the constant compliance lines of the inward and outward traces of the force run. Hence, neither specific friction measurements nor torsional calibration are required. The fact that the lateral results agree with those obtained with the axial method shows that the new method is successful. While the resolution of single force curve measurements is slightly poorer than for the lateral method, this should be easily addressed by averaging multiple runs. The technique has the potential to be useful not only for older AFMs not having the capacity to measure lateral forces, but also in environments where friction behaviour might be expected to change rather rapidly with time – the entire friction-load relationship can be captured in a single force curve – i.e. considerably less than a second if necessary

8 Acknowledgement

I would like to express my sincere gratitude and gratefulness to all the people who have helped and supported me while working with this thesis. To mention a few, though not forgetting anyone – you are all in my mind – I would like to mention the following:

Fredrik Tiberg, for providing the opportunity for me to work scientifically with cellulose.

Mark Rutland, for the scientific guidance.

Johan Fröberg, for introducing me to the MASIF world, DLVO theory and EndNote.

BiMaC, the Biofibre Materials Centre at KTH, for financial support, and for facilitating cooperative research.

The co-authors of the included papers, for good cooperation.

Present and former colleagues at the Fundamental Surface Science Group and YKI, for creating a good working environment and supporting atmosphere.

Katarina Theander, for fruitful discussion about surface forces, cellulose and life.

My family and friends, who I have been way too bad in keeping in contact with – Please forgive me.

Anders and Agnes, for being the sunshine of my life and making it all worthwhile.

9 References

1. Ducker, W. A.; Senden, T. J.; Pashley, R. M., *Direct Measurement of Colloidal Forces Using an Atomic Force Microscope*. *Nature*, 1991, 353, 239-241.
2. Ducker, W. A.; Senden, T. J.; Pashley, R. M., *Measurement of Forces in Liquids Using a Force Microscope*. *Langmuir*, 1992, 8, 1831-1836.
3. Neuman, R. D.; Berg, J. M.; Claesson, P. M., *Direct measurement of surface forces in papermaking and paper coating systems*. *Nordic Pulp Paper Res. J.*, 1993, 8, 96-104.
4. Holmberg, M.; Berg, J.; Stemme, S.; Odberg, L.; Rasmusson, J.; Claesson, P., *Surface force studies of Langmuir-Blodgett cellulose films*. *J. Colloid Interface Sci.*, 1997, 186, 369-381.
5. Holmberg, M.; Wigren, R.; Erlandsson, R.; Claesson, P. M., *Interactions between cellulose and colloidal silica in the presence of polyelectrolytes*. *Colloids Surf. A*, 1997, 130, 175-183.
6. Rutland, M. W.; Carambassis, A.; Willing, G. A.; Neuman, R. D., *Surface force measurements between cellulose surfaces using scanning probe microscopy*. *Colloids Surf. A*, 1997, 123, 369-374.
7. Carambassis, A.; Rutland, M. W., *Interactions of cellulose surfaces: Effect of electrolyte*. *Langmuir*, 1999, 15, 5584-5590.
8. Zauscher, S.; Klingenberg, D. J., *Normal forces between cellulose surfaces measured with colloidal probe microscopy*. *J. Colloid Interface Sci.*, 2000, 229, 497-510.
9. Zauscher, S.; Klingenberg, D. J., *Friction between cellulose surfaces measured with colloidal probe microscopy*. *Colloids Surf. A*, 2001, 178, 213-229.
10. Notley, S. M.; Pettersson, B.; Wagberg, L., *Direct measurement of attractive van der Waals' forces between regenerated cellulose surfaces in an aqueous environment*. *J. Am. Chem. Soc.*, 2004, 126, 13930-13931.
11. Notley, S. M.; Wagberg, L., *Morphology of modified regenerated model cellulose II surfaces studied by atomic force microscopy: Effect of carboxymethylation and heat treatment*. *Biomacromolecules*, 2005, 6, 1586-1591.
12. Theander, K.; Pugh, R. J.; Rutland, M. W., *Friction force measurements relevant to de-inking by means of atomic force microscope*. *J. Colloid Interface Sci.*, 2005, 291, 361-368.
13. Christiernin, M.; Henriksson, G.; Lindstrom, M. E.; Brumer, H.; Teeri, T. T.; Lindstrom, T.; Laine, J., *The effects of xyloglucan on the properties of paper made from bleached kraft pulp*. *Nordic Pulp Paper Res. J.*, 2003, 18, 182-187.
14. Lima, D. U.; Oliveira, R. C.; Buckeridge, M. O., *Seed storage hemicelluloses as wet-end additives in papermaking*. *Carbohydrate Polymers*, 2003, 52, 367-373.
15. Israelachvili, J. *Intermolecular and Surface Forces*; Second Edition ed.; Academic Press: San Diego, 1992.
16. Derjaguin, B. V., *Kolloid-Z*, 1934, 69, 155-164.
17. Derjaguin, B. V.; Landau, L., *Acta Physiochim.*, 1941, 14, 633-662.

18. Verwey, E. J. W.; Overbeek, J. T. G. *Theory of the stability of lyophobic colloids : the interaction of sol particles having an electric double layer*; Elsevier: New York, 1948.
19. Bostrom, M.; Williams, D. R. M.; Ninham, B. W., *Specific ion effects: Why DLVO theory fails for biology and colloid systems*. Phys. Rev. Lett., 2001, 8716.
20. Horn, R. G.; Smith, D. T.; Haller, W., *Surface Forces and Viscosity of Water Measured between Silica Sheets*. Chem. Phys. Lett., 1989, 162, 404-408.
21. Israelachvili, J. N.; Wennerstrom, H., *Hydration or Steric Forces between Amphiphilic Surfaces*. Langmuir, 1990, 6, 873-876.
22. Gibbs, J. W. *The collected works of J. W. Gibbs*; Green: New York, 1931; Vol. 1.
23. Akesson, T.; Woodward, C.; Jonsson, B., *Electric Double-Layer Forces in the Presence of Poly-Electrolytes*. J. Chem. Phys., 1989, 91, 2461-2469.
24. Rand, R. P.; Fuller, N. L.; Lis, L. J., *Myelin Swelling and Measurement of Forces between Myelin Membranes*. Nature, 1979, 279, 258-260.
25. Plunkett, M. A.; Feiler, A.; Rutland, M. W., *Atomic force microscopy measurements of adsorbed polyelectrolyte layers. 2. Effect of composition and substrate on structure, forces, and friction*. Langmuir, 2003, 19, 4180-4187.
26. Gao, J. P.; Luedtke, W. D.; Gourdon, D.; Ruths, M.; Israelachvili, J. N.; Landman, U., *Frictional forces and Amontons' law: From the molecular to the macroscopic scale*. J. Phys. Chem. B, 2004, 108, 3410-3425.
27. Feiler, A.; Jenkins, P.; Rutland, M. W., *Effect of relative humidity on adhesion and frictional properties of micro- and nano-scopic contacts*. J. Adhes. Sci. Technol., 2005, 19, 165-179.
28. Lokar, W. J.; Ducker, W. A., *Proximal adsorption of dodecyltrimethylammonium bromide to the silica-electrolyte solution interface*. Langmuir, 2002, 18, 3167-3175.
29. Subramanian, V.; Ducker, W., *Proximal adsorption of cationic surfactant on silica at equilibrium*. J. Phys. Chem. B, 2001, 105, 1389-1402.
30. Pethica, B. A., *Adsorption equilibria in surface force balance studies*. Colloids Surf. A, 1995, 105, 257-264.
31. Podgornik, R.; Parsegian, V. A., *Forces between Ctab-Covered Glass Surfaces Interpreted as an Interaction-Driven Surface Instability*. J. Phys. Chem., 1995, 99, 9491-9496.
32. Yaminsky, V. V.; Ninham, B. W.; Christenson, H. K.; Pashley, R. M., *Adsorption forces between hydrophobic monolayers*. Langmuir, 1996, 12, 1936-1943.
33. Christenson, H. K.; Yaminsky, V. V., *Is the long-range hydrophobic attraction related to the mobility of hydrophobic surface groups?* Colloids Surf. A, 1997, 130, 67-74.
34. Parker, J. L., *A Novel Method For Measuring the Force Between 2 Surfaces in a Surface Force Apparatus*. Langmuir, 1992, 8, 551-556.
35. Parker, J. L., *Surface Force Measurements in Surfactant Systems*. Progress in Surface Science, 1994, 47, 205-271.
36. Israelachvili, J. N.; Tabor, D., *The measurement of van der Waals dispersion forces in the range of 1.5 to 130 nm*. Proc. R. Soc. Lond., 1972, A331, 19-38.
37. Senden, T. J., *Force microscopy and surface interactions*. Curr. Opin. Colloid Interface Sci., 2001, 6, 95-101.

38. Binnig, G.; Quate, C. F.; Gerber, C., *Atomic Force Microscope*. Phys. Rev. Lett., 1986, 56, 930-933.
39. Cleveland, J. P.; Manne, S.; Bocek, D.; Hansma, P. K., *A Nondestructive Method for Determining the Spring Constant of Cantilevers for Scanning Force Microscopy*. Rev. Sci. Instrum., 1993, 64, 403-405.
40. Hutter, J. L.; Bechhoefer, J., *Calibration of Atomic-Force Microscope Tips*. Rev. Sci. Instrum., 1993, 64, 1868-1873.
41. Butt, H. J.; Jaschke, M., *Calculation of Thermal Noise in Atomic-Force Microscopy*. Nanotechnology, 1995, 6, 1-7.
42. Sader, J. E.; Chon, J. W. M.; Mulvaney, P., *Calibration of rectangular atomic force microscope cantilevers*. Rev. Sci. Instrum., 1999, 70, 3967-3969.
43. Levy, R.; Maaloum, M., *Measuring the spring constant of atomic force microscope cantilevers: thermal fluctuations and other methods*. Nanotechnology, 2002, 13, 33-37.
44. Sader, J. E., *Frequency response of cantilever beams immersed in viscous fluids with applications to the atomic force microscope*. Journal of Applied Physics, 1998, 84, 64-76.
45. Hertz, H., *Ueber die Berührung fester elastischer Körper*. J. Reine Angew. Math., 1881, 92, 156-171.
46. Johnson, K. L.; Kendall, K.; Roberts, A. D., *Surface energy and the contact of elastic solids*. Proc. R. Soc. Lond., 1971, A324, 301-313.
47. Derjaguin, B. V.; Muller, V. M.; Toporov, Y. P., *Effect of Contact Deformations on Adhesion of Particles*. J. Colloid Interface Sci., 1975, 53, 314-326.
48. Rutland, M. W.; Tyrrell, J. W. G.; Attard, P., *Analysis of atomic force microscopy data for deformable materials*. J. Adhes. Sci. Technol., 2004, 18, 1199-1215.
49. Bogdanovic, G.; Meurk, A.; Rutland, M. W., *Tip friction - torsional spring constant determination*. Colloids Surf. B, 2000, 19, 397-405.
50. Feiler, A.; Attard, P.; Larson, I., *Calibration of the torsional spring constant and the lateral photodiode response of frictional force microscopes*. Rev. Sci. Instrum., 2000, 71, 2746-2750.
51. Ecke, S.; Raiteri, R.; Bonaccorso, E.; Reiner, C.; Deiseroth, H. J.; Butt, H. J., *Measuring normal and friction forces acting on individual fine particles*. Rev. Sci. Instrum., 2001, 72, 4164-4170.
52. Ogletree, D. F.; Carpick, R. W.; Salmeron, M., *Calibration of frictional forces in atomic force microscopy*. Rev. Sci. Instrum., 1996, 67, 3298-3306.
53. Cain, R. G.; Biggs, S.; Page, N. W., *Force calibration in lateral force microscopy*. J. Colloid Interface Sci., 2000, 227, 55-65.
54. Pietrement, O.; Beaudoin, J. L.; Troyon, M., *A new calibration method of the lateral contact stiffness and lateral force using modulated lateral force microscopy*. Tribology Letters, 1999, 7, 213-220.
55. Liu, E.; Blanpain, B.; Celis, J. P., *Calibration procedures for frictional measurements with a lateral force microscope*. Wear, 1996, 192, 141-150.
56. Liu, Y. H.; Evans, D. F.; Song, Q.; Grainger, D. W., *Structure and frictional properties of self-assembled surfactant monolayers*. Langmuir, 1996, 12, 1235-1244.

57. Liu, Y. H.; Wu, T.; Evans, D. F., *Lateral Force Microscopy Study on the Shear Properties of Self-Assembled Monolayers of Dialkylammonium Surfactant on Mica*. *Langmuir*, 1994, 10, 2241-2245.
58. Ederth, T.; Claesson, P. M.; Liedberg, B., *Self-assembled monolayers of alkanethiolates on thin gold films as substrates for surface force measurements. Long-range hydrophobic interactions and electrostatic double-layer interactions*. *Langmuir*, 1998, 14, 4782-4789.
59. Falt, S.; Wagberg, L.; Vesterlind, E. L.; Larsson, P. T., *Model films of cellulose II - improved preparation method and characterization of the cellulose film*. *Cellulose*, 2004, 11, 151-162.
60. Beck-Candanedo, S.; Roman, M.; Gray, D. G., *Effect of reaction conditions on the properties and behavior of wood cellulose nanocrystal suspensions*. *Biomacromolecules*, 2005, 6, 1048-1054.
61. Edgar, C. D.; Gray, D. G., *Smooth model cellulose I surfaces from nanocrystal suspensions*. *Cellulose*, 2003, 10, 299-306.
62. Mukerjee, P.; Mysels, K. J. *Critical Micelle Concentrations of Aqueous Surfactant Systems*; US Department of Commerce, National Bureau of Standards: Washington, 1970; Vol. NSRDS-NBS 36.
63. Sepulveda, L.; Cortes, J., *Ionization Degrees and Critical Micelle Concentrations of Hexadecyltrimethylammonium and Tetradecyltrimethylammonium Micelles with Different Counterions*. *J. Phys. Chem.*, 1985, 89, 5322-5324.
64. Bergstrom, L.; Stemme, S.; Dahlfors, T.; Arwin, H.; Odberg, L., *Spectroscopic ellipsometry characterisation and estimation of the Hamaker constant of cellulose*. *Cellulose*, 1999, 6, 1-13.
65. Herrington, T. M.; Petzold, J. C., *An Investigation into the Nature of Charge on the Surface of Papermaking Woodpulp .1. Charge Ph Isotherms*. *Colloids Surf.*, 1992, 64, 97-108.
66. Chan, D. Y. C.; Pashley, R. M.; White, L. R., *A Simple Algorithm for the Calculation of the Electrostatic Repulsion between Identical Charged Surfaces in Electrolyte*. *J. Colloid Interface Sci.*, 1980, 77, 283-285.
67. Bell, G. M.; Peterson, G. C., *Calculation of the Electric Double-Layer Force Between Unlike Spheres*. *J. Colloid Interface Sci.*, 1972, 41, 542-566.
68. Devereux, O. F.; de Bruyn, P. L. *Interaction of Plane-Parallel Double Layers*; MIT Press: Cambridge, 1963.
69. Fisher, L. R.; Israelachvili, J. N., *Direct experimental verification of the Kelvin equation for capillary condensation*. *Nature (London, United Kingdom)*, 1979, 277, 548-549.
70. Ata, A.; Rabinovich, Y. I.; Singh, R. K., *role of surface roughness in capillary adhesion*. *J. Adhesion Sci. Technol*, 2002, 16, 337-346.
71. Rabinovich, Y. I.; Adler, J. J.; Ata, A.; Singh, R. K.; Moudgil, B. M., *Adhesion between nanoscale rough surfaces II measurement and comparison with theory*. *J. Colloid Interface Sci*, 2000, 232, 17-24.
72. Benson, R. E., *Effects of Relative Humidity and Temperature on Tensile Stress-Strain Properties of Kraft Linerboard*. *Tappi*, 1971, 54, 699-703.
73. Scott, W. E. *Properties of Paper: An Introduction*; TAPPI Press: Atlanta, 1989.

74. Fellers, C.; Norman, B. *Pappersteknik*; Avdelningen för Pappersteknik, KTH: Stockholm, 1998.
75. Cosgrove, D. J., *Growth of the plant cell wall*. Nature Reviews Molecular Cell Biology, 2005, 6, 850-861.
76. Thompson, D. S., *How do cell walls regulate plant growth?* Journal of Experimental Botany, 2005, 56, 2275-2285.
77. Somerville, C.; Bauer, S.; Brininstool, G.; Facette, M.; Hamann, T.; Milne, J.; Osborne, E.; Paredez, A.; Persson, S.; Raab, T.; Vorwerk, S.; Youngs, H., *Toward a systems approach to understanding plant-cell walls*. Science, 2004, 306, 2206-2211.
78. Hayashi, T., *Xyloglucans in the Primary-Cell Wall*. Annual Review of Plant Physiology and Plant Molecular Biology, 1989, 40, 139-168.
79. Fry, S. C., *The Structure and Functions of Xyloglucan*. Journal of Experimental Botany, 1989, 40, 1-11.
80. Hayashi, T.; Maclachlan, G., *Pea Xyloglucan and Cellulose .1. Macromolecular Organization*. Plant Physiology, 1984, 75, 596-604.
81. Levy, S.; York, W. S.; Stuikeprill, R.; Meyer, B.; Staehelin, L. A., *Simulations of the Static and Dynamic Molecular-Conformations of Xyloglucan - the Role of the Fucosylated Side-Chain in Surface-Specific Side-Chain Folding*. Plant J., 1991, 1, 195-215.
82. Hayashi, T.; Ogawa, K.; Mitsuishi, Y., *Characterization of the Adsorption of Xyloglucan to Cellulose*. Plant and Cell Physiology, 1994, 35, 1199-1205.
83. Whitney, S. E. C.; Brigham, J. E.; Darke, A. H.; Reid, J. S. G.; Gidley, M. J., *In-Vitro Assembly of Cellulose/Xyloglucan Networks - Ultrastructural and Molecular Aspects*. Plant J., 1995, 8, 491-504.
84. Vincken, J. P.; Dekeizer, A.; Beldman, G.; Voragen, A. G. J., *Fractionation of Xyloglucan Fragments and Their Interaction with Cellulose*. Plant Physiology, 1995, 108, 1579-1585.
85. Brumer, H.; Zhou, Q.; Baumann, M. J.; Carlsson, K.; Teeri, T. T., *Activation of crystalline cellulose surfaces through the chemoenzymatic modification of xyloglucan*. J. Am. Chem. Soc., 2004, 126, 5715-5721.
86. Zhou, Q.; Greffe, L.; Baumann, M. J.; Malmstrom, E.; Teeri, T. T.; Brumer, H., *Use of xyloglucan as a molecular anchor for the elaboration of polymers from cellulose surfaces: A general route for the design of biocomposites*. Macromolecules, 2005, 38, 3547-3549.
87. Ludwig, M.; Rief, M.; Schmidt, L.; Li, H.; Oesterhelt, F.; Gautel, M.; Gaub, H. E., *AFM, a tool for single-molecule experiments*. Applied Physics a-Materials Science & Processing, 1999, 68, 173-176.
88. Fisher, T. E.; Marszalek, P. E.; Fernandez, J. M., *Stretching single molecules into novel conformations using the atomic force microscope*. Nature Structural Biology, 2000, 7, 719-724.
89. Parker, J. L.; Rutland, M. W., *Time-Dependent Adhesion Between Glass Surfaces in Dilute Surfactant Solutions*. Langmuir, 1993, 9, 1965-1967.
90. Plunkett, M. A.; Rutland, M. W., *Dynamic adhesion of grafted polymer surfaces as studied by surface force measurements*. J. Adhes. Sci. Technol., 2002, 16, 983-996.

91. Derjaguin, B. V.; Toporov, Y. P., *Influence of Adhesion on the Sliding and Rolling Friction*. Progress in Surface Science, 1994, 45, 317-327.
92. Carpick, R. W.; Ogletree, D. F.; Salmeron, M., *A general equation for fitting contact area and friction vs load measurements*. J. Colloid Interface Sci., 1999, 211, 395-400.
93. Feiler, A.; Larson, I.; Jenkins, P.; Attard, P., *A quantitative study of interaction forces and friction in aqueous colloidal systems*. Langmuir, 2000, 16, 10269-10277.
94. Bogdanovic, G.; Tiberg, F.; Rutland, M. W., *Sliding friction between cellulose and silica surfaces*. Langmuir, 2001, 17, 5911-5916.
95. Feiler, A.; Plunkett, M. A.; Rutland, M. W., *Atomic force microscopy measurements of adsorbed polyelectrolyte layers. 1. Dynamics of forces and friction*. Langmuir, 2003, 19, 4173-4179.
96. Berg, I. C. H.; Rutland, M. W.; Arnebrant, T., *Lubricating properties of the initial salivary pellicle - an AFM Study*. Biofouling, 2003, 19, 365-369.
97. Parker, J. L.; Yaminsky, V. V.; Claesson, P. M., *Surface Forces Between Glass Surfaces in Cetyltrimethylammonium Bromide Solutions*. J. Phys. Chem., 1993, 97, 7706-7710.
98. Rutland, M. W.; Parker, J. L., *Surface Forces Between Silica Surfaces in Cationic Surfactant Solutions - Adsorption and Bilayer Formation At Normal and High Ph*. Langmuir, 1994, 10, 1110-1121.
99. Wängnerud, P.; Olofsson, G., *Adsorption Isotherms for Cationic Surfactants on Silica Determined by in Situ Ellipsometry*. J. Colloid Interface Sci., 1992, 153, 392-398.
100. Wängnerud, P.; Jonsson, B., *Adsorption of Ionic Amphiphiles As Bilayers On Charged Surfaces*. Langmuir, 1994, 10, 3268-3278.
101. Yaminsky, V. V.; Ninham, B. W.; Stewart, A. M., *Surface activity and ion exchange. A study via surface tension, wetting tension, and surface force techniques*. Langmuir, 1996, 12, 836-850.
102. Eskilsson, K.; Ninham, B. W.; Tiberg, F.; Yaminsky, V. V., *Effects of adsorption of low-molecular-weight triblock copolymers on interactions between hydrophobic surfaces in water*. Langmuir, 1999, 15, 3242-3249.